The Dynamics of the India-Eurasia Collision: Faulted Viscous Continuum Models Constrained by High-Resolution Sentinel-1 InSAR and GNSS Velocities

Jin Fang[1], Gregory A. Houseman[1], Tim J. Wright[1], Lynn A. Evans[2], Tim J. Craig[1], John R. Elliott[1], and Andy Hooper[1]

[1]COMET, School of Earth and Environment, University of Leeds, Leeds, United Kingdom
[2]School of Earth, Atmosphere and Environment, Monash University, Clayton, Australia

Key Points:

- A suite of faulted viscous shell models testing key parameters explain new observations from geodesy for the India-Eurasia collision.
- The India-Eurasia collision is explained by the balance between buoyancy and boundary forces, slip-resistance on major faults, and internal viscosity variations.
- Central Tibetan Plateau has a vertically-averaged effective viscosity of $\sim 10^{21}$ Pa s, 1-2 orders lower than the surrounding area.

Corresponding author: Jin Fang, `eejf@leeds.ac.uk`

Abstract
The dynamics of lithospheric deformation in the India-Eurasia collision zone has been debated over many decades. Here we test a two-dimensional (2-D) Thin Viscous Shell (TVS) approach that has been adapted to explicitly account for displacement on major faults and investigate the impact of lateral variations in depth-averaged lithospheric strength. We present a suite of dynamic models to explain the key features from new high-resolution Sentinel-1 Interferometric Synthetic Aperture Radar (InSAR) as well as Global Navigation Satellite System (GNSS) velocities. Comparisons between calculated and geodetically observed velocity and strain rate fields indicate: (a) internal buoyancy forces from Gravitational Potential Energy (GPE) acting on a relatively weak region of highest topography (>2,000 m) contribute to dilatation of the high plateau and contraction on the margins; (b) a weak central Tibetan Plateau ($\sim 10^{21}$ Pa s compared to far-field depth-averaged effective viscosity of 10^{22} to 10^{23} Pa s) is required to explain the observed long-wavelength eastward velocity variation away from major faults; (c) slip on faults produces strain localization and clockwise rotation around the Eastern Himalayan Syntaxis (EHS). We discuss the tectonic implications for rheology of the lithosphere, distribution of geodetic strain, and partitioning of active faulting and seismicity.

Plain Language Summary

The collision of the Indian Plate with Eurasia has created the Tibetan Plateau, the largest deforming region in the continents. It has been a focus for heated debate and has inspired two contrasting tectonic models: (a) The deformation is localized on major faults separating "blocks" or (b) the strain is distributed throughout a "continuum". We approximate the India-Eurasia collision by treating the continent as a two-dimensional viscous fluid with regional variations in strength, explicitly accounting for displacements on selected major faults. We present a suite of models to explain the key features of new observations from satellites. The best-fit model involves a weak Tibetan Plateau, a particularly weaker central Plateau, and four strong regions outside the Plateau, and requires resistance to slip on faults. This represents the deformation field of the India-Eurasia collision zone as a combination of continuous distributed deformation and focused strain on major faults.

1 Introduction

The Tibetan Plateau was created by the collision of the Indian Plate with Eurasia and has long been a testing ground for models of continental deformation. It extends more than 2,000 km north of the Himalayan Frontal Thrust, where large active faults appear to have developed since middle Miocene (Duvall et al., 2013). Geodetic observations from Global Navigation Satellite System (GNSS) and Interferometric Synthetic Aperture Radar (InSAR) reveal a complex pattern of current deformation in the India-Eurasia collision zone (Figure 1). The Tibetan Plateau and its margins accommodate India's indentation into Eurasia by crustal shortening, widespread active faulting, folding and uplifting (Q. Wang et al., 2001). In the Eurasia fixed reference frame, the westward motion in the western Tibetan Plateau is tapered to zero while the eastward velocities increase over ∼1,000 km distance across the eastern plateau before decreasing rapidly outside the plateau (M. Wang & Shen, 2020). Deformation within the plateau and the Tian Shan to the north is broadly distributed whereas outside these areas there are large undeforming regions with deformation focused around the perimeter of these regions (Ge et al., 2015; Zheng et al., 2017; M. Wang & Shen, 2020; W. Li et al., 2022). One of these undeforming regions, the Tarim Basin between the plateau and Tian Shan, has been observed to rotate clockwise at a rate of 0.4-0.6 °/Myr with respect to Eurasia since the Cenozoic era (Avouac & Tapponnier, 1993; Z.-K. Shen et al., 2001; Craig et al., 2012; J. Zhao et al., 2019; M. Wang & Shen, 2020).

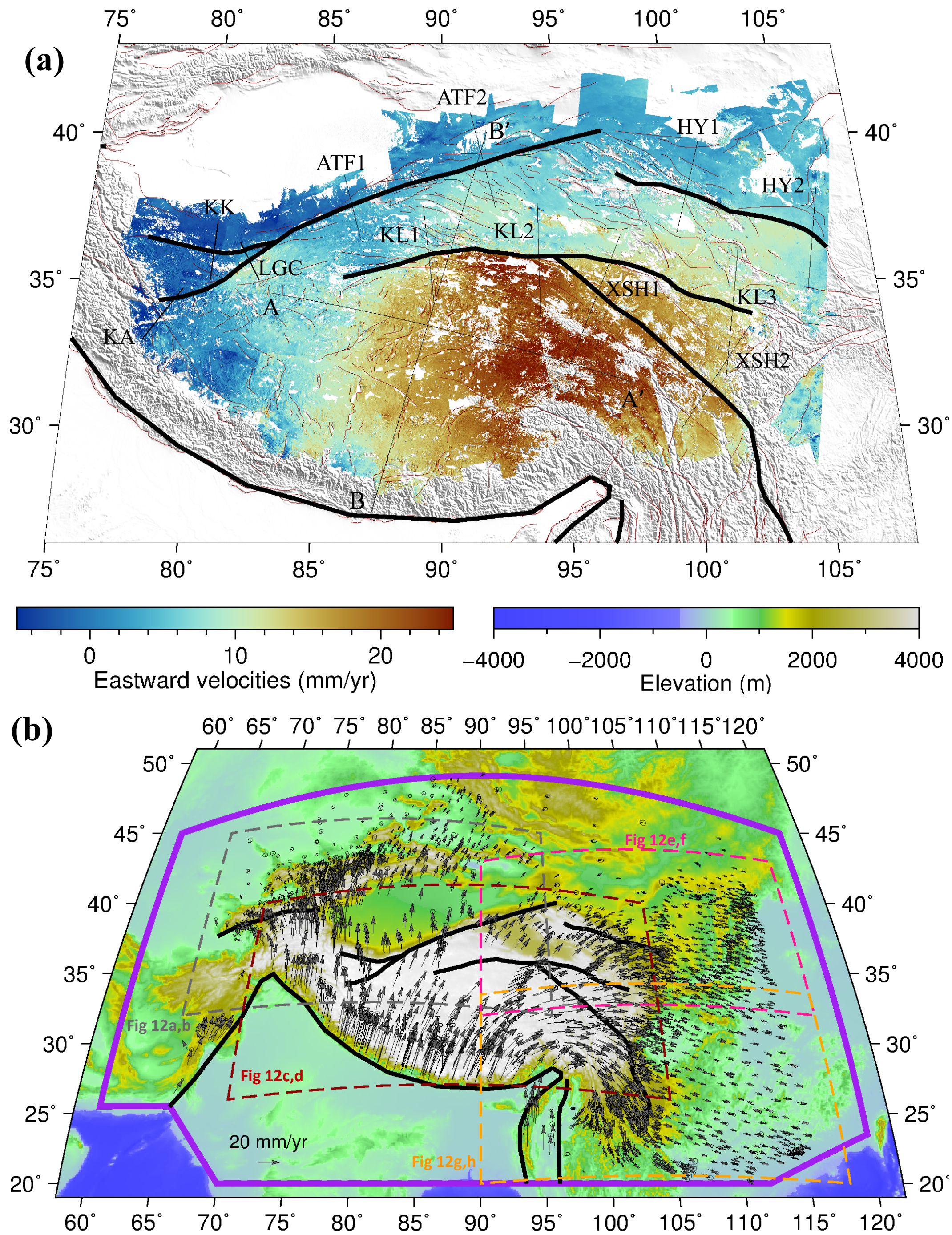

Figure 1. (a) Eastward velocity map constructed from ascending and descending Sentinel-1 InSAR line-of-sight velocities (Wright et al., 2023). Black lines show the location of profiles presented in Figure 6. Dark red lines are fault traces from the Global Earthquake Model (GEM) Global Active Faults Database (Styron & Pagani, 2020). Thick black lines are model faults incorporated in numerical simulations in this study. Abbreviation of names for fault profiles: KA = Karakoram Fault, KK = Karakash Fault, LGC = Longmu-Gozha Co Fault, ATF = Altyn Tagh Fault, HY = Haiyuan Fault, KL = Kunlun Fault, XSH = Xianshuihe Fault. (b) GNSS velocities (Wright et al., 2023, and references therein). Purple polygon shows the boundary of calculation domain. Dashed lines show the extents of zoomed view shown in Figure 12. Thick black lines are model faults incorporated in this study.

While some major strike-slip faults in the Tibetan Plateau show strain concentrations (Kreemer et al., 2014; Ge et al., 2015), there are also areas of diffuse strain (Zheng et al., 2017). The high plateau is dilating at a rate of ∼10-20 nanostrain/yr (Molnar & Deng, 1984; Ge et al., 2015; Zheng et al., 2017; Wright et al., 2021, 2022, 2023). WNW-ESE extension occurs throughout the plateau interior through a set of north-south striking rifts/grabens and conjugate strike-slip faulting (Molnar & Tapponnier, 1978; Duvall et al., 2013; H. Wang et al., 2019); the northern and southern regions of the Tibetan Plateau show similar rates of dilatation in short-term geodetic data (Ge et al., 2015), although geological data suggest arc-parallel extension rates in the plateau may be higher nearer the Himalayan arc (Copley et al., 2011). The northeastern Tibetan Plateau and the eastern and southern margins of the plateau, as well as the Tian Shan region, are experiencing rapid contraction (Molnar & Tapponnier, 1978; Q. Wang et al., 2001; England & Molnar, 2015; Y. Li et al., 2018; Metzger et al., 2020, 2021; J. Li et al., 2022; Ou et al., 2022; Zhu et al., 2022). The southeastern Tibetan Plateau rotates clockwise around the eastern Himalayan syntaxis (EHS) (Q. Wang et al., 2001; Z. Shen et al., 2005; W. Wang et al., 2017; Zheng et al., 2017; Y. Li et al., 2019; M. Wang & Shen, 2020; Gan et al., 2021; W. Wang et al., 2021).

How best to understand the deformation field produced by the India-Asia collision has been a subject of extensive debate (Thatcher, 2009; Searle et al., 2011; Bendick & Flesch, 2013; P. Zhang, 2013; H. Zhang et al., 2020; Dal Zilio et al., 2021). Since the early days of plate tectonics, which beautifully explains the motion of oceanic plates, it has been recognized that deformation of the continents cannot be described by the motion of only a few large plates, with seismicity focused around their edges (McKenzie, 1972). Nevertheless, a popular approach for characterizing continental deformation is to model the deformation as rotation and translation of a number of blocks, or microplates, each following the kinematic rules of plate tectonics (Avouac & Tapponnier, 1993; McCaffrey et al., 2000; McClusky et al., 2001; Wallace et al., 2004; Meade & Hager, 2005; Wallace et al., 2005; Socquet et al., 2006; Thatcher, 2007; W. Wang et al., 2017; Y. Li et al., 2018; W. Wang et al., 2021). In most formulations of block models, strain concentrations only occur along the block boundaries, although a few allow for strain within block interiors (Q. Chen et al., 2004; Loveless & Meade, 2011). Avouac and Tapponnier (1993) proposed the first 4-microplate model for the India-Asia collision based primarily on geological observations. Q. Chen et al. (2004) constructed a deformable block model to explain GNSS observations from 45 stations. The trend in subsequent models has been to increase the number of blocks to fit more GNSS observations as they become available (Thatcher, 2007; Loveless & Meade, 2011; W. Wang et al., 2017; Y. Li et al., 2018; W. Wang et al., 2021; Styron, 2022). These block models are helpful for deriving slip rates and locking depths for major faults and are widely used in seismic hazard analysis (W. Wang et al., 2017; Y. Li et al., 2018; W. Wang et al., 2021; Styron, 2022). They can naturally describe large undeforming areas and focused strain around faults. If enough blocks are used, these models can reproduce any observed features of the strain field. However, because the models are purely kinematic, they have no predictive power and cannot be used to test the underlying causes of the observed deformation or to understand the balance of forces acting on blocks. The geodetic strain can be described in the short term, even with an elastic model, but appealing to elastic strain as an explanation of strain rates sustained on geological time-scales is not logically self-consistent. In addition, as focused strain might not coincide with mapped faults (H. Wang & Wright, 2012; H. Wang et al., 2019), a simple block model could underestimate the likelihood of earthquakes occurring on unknown faults due to our imperfect knowledge of the boundaries of crustal blocks, which must be defined a priori; all earthquakes by definition must occur on block boundaries in such a framework.

An alternative approach has been to treat continents as a continuum, with deformation modeled as a viscous fluid acting under the influence of the internal and boundary forces applied, and a simply parameterized viscous constitutive law (England & McKenzie, 1982; Flesch et al., 2001). In these models, deformation is distributed throughout the layer representing the lithosphere. England and McKenzie (1982) simplified the deformation to a two-dimensional (2-D) problem by treating the lithosphere as a thin viscous sheet originally developed for a flat layer with vertically-averaged properties. England and Houseman (1986) applied the viscous sheet formulation assuming a uniform viscosity coefficient to analyze the dynamics of the India-Eurasia collision. In such models, strain is focused where gradients of Gravitational Potential Energy (GPE) are greatest, and on parts of the boundary where the boundary forces change rapidly. With more and more observations and stronger computational power, more complexity in models has been required to explain the observations (Neil & Houseman, 1997; Flesch et al., 2001; Vergnolle et al., 2007; Lechmann et al., 2014; Bischoff & Flesch, 2018, 2019). Early viscous continuum models did not predict the strain concentrations observed in dense geodetic data around major faults. However, Dayem et al. (2009) and Molnar and Dayem (2010) showed that viscous continuum models can concentrate strain at regions of strength contrast. Lechmann et al. (2014) and Bischoff and Flesch (2018, 2019) achieved strain concentrations by explicitly allowing weaker regions to represent localized strain associated with major faults.

The lower crust is expected to be relatively weak based on typical power law creep laws (Brace & Kohlstedt, 1980). Some authors have argued that the lower crust is so weak that it is decoupled from both the upper crust and the upper mantle. W. Zhao and Morgan (1987) presented a model in which the stronger Indian crust injects into the weaker fluid-like lower crust of the Tibetan Plateau. Based on geologic and GNSS observations, Royden et al. (1997, 2008) presented a lower crustal flow model in the eastern Tibetan Plateau where crustal material flows around the EHS and also around the strong Sichuan Basin. They argued that the lower crust escapes from beneath the central plateau through regions where crust is weak (Clark & Royden, 2000), and that the morphology of the eastern plateau reflects crustal material flows. Copley and McKenzie (2007) interpreted the formation of the geometry of the EHS by gravitationally driven fluid flow in both the southern Tibetan Plateau and the Indo-Burman Ranges. Bischoff and Flesch (2019) approximated the three-dimensional (3-D) India-Eurasia deformation with creeping flow, with a weak lower crust required to explain the observed vertical surface velocities. However, Rey et al. (2010) show that large-scale relative displacement of the lower and upper crust is unlikely. Their result justifies a key assumption of the TVS method that the lithosphere deforms coherently with depth, that is, horizontal velocity is independent of depth and horizontal tractions can be vertically averaged.

Lower crustal channel flow has also been invoked for models in which material in a partially molten mid-crust is extruded southward from beneath the southern Tibetan Plateau towards the high Himalayan slab (Grujic et al., 2002; Searle et al., 2003; Law et al., 2004; Searle & Szulc, 2005; Godin et al., 2006; Searle et al., 2006, 2011). Beaumont et al. (2001) interpreted the Himalayan tectonics by a low-viscosity channel flow and ductile extrusion; high-grade metamorphic rocks were exhumed from this channel. However, Copley et al. (2011) argued that the mechanical coupling between the upper crust of the southern Tibetan Plateau and the underthrust Indian crust is inconsistent with the low-viscosity 'channel flow' models in the southern plateau. Flesch et al. (2018) suggest surface GNSS velocities contain little or no information about 3-D dynamics. Penney and Copley (2021) further suggest that the temporal evolution of topography in the southeastern Tibetan Plateau can be explained without invoking a low-viscosity lower crustal channel.

Both block models and continuum models are over-simplifications of a more complex reality that requires both distributed deformation and, at least in the near surface, slip on faults (Thatcher, 2009). Ductile deformation is manifested in almost any geological environment where the temperatures are sufficiently great, but near surface deformation typically occurs by faulting. In the case of large-scale continental faults, seismic activity is typically restricted to the upper 15 km or so (Wright et al., 2013), but there is increasing evidence that localized deformation is moderated by ductile shear zones that can extend through the crustal layer and possibly into the mantle (Warner, 1990; Kelemen & Dick, 1995; Leloup et al., 1999; Thybo et al., 2000; Bürgmann & Dresen, 2008; Vauchez et al., 2012; Alvizuri & Hetényi, 2019; Scholz & Choi, 2022). Hence the deformation field in general can be represented as a continuum modulated by major faults. Continuum models are appealing in that they have the potential to explain large-scale deformation with relatively few adjustable parameters. Garthwaite and Houseman (2011) demonstrate the validity of the 2-D thin viscous sheet approximation for continental collision provided that the indenter width is larger than the thickness of the lithosphere. In this study, we employ the adapted 2-D TVS continuum model of England and McKenzie (1982), explicitly modified to account for displacement discontinuities on faults. Although a linear constitutive relation between stress and strain rate is often adopted in 3-D numerical modeling (Royden et al., 1997; F. Shen et al., 2001; Liu & Yang, 2003; Copley & McKenzie, 2007; Lechmann et al., 2014; Bischoff & Flesch, 2019; Penney & Copley, 2021), we assume a non-Newtonian (power law) viscous rheology. Early geodynamic simulations have primarily relied on information from topography, Quaternary fault slip rates, and seismic moment tensors. The constantly-improving accuracy and resolution of the geodetic observations now enable tighter constraints on tectonic models. We present a suite of faulted viscous continuum models constrained by new geodetic observations of the India-Eurasia collision. This allows us to explore (a) the importance of internal buoyancy forces from GPE, (b) the relationship between slip resistance on faults and associated ductile deformation, and (c) the role of rheological/strength contrasts and how they modulate and localize deformation.

2 Data and Methods

2.1 Data

We use constraints from new high-resolution InSAR and published GNSS horizontal velocity fields (Wright et al., 2023, and references therein, Figure 1) to test the faulted viscous continuum model. Both datasets are fixed to a Eurasia reference frame. As relative motion across the Himalaya and Indo-Burma subduction zones appears to be controlled by 3-D geometry (Ni et al., 1989; C. Li et al., 2008b; Liang et al., 2016; Dubey et al., 2022), we do not incorporate measurements within the Indian Plate in our 2-D dynamic modeling. We obtain a relatively sparse set of velocity vectors by a weighted average of joint model velocities of InSAR and GNSS (Wright et al., 2023) derived from the VELMAP approach (H. Wang & Wright, 2012). We sub-sample the combined geodetic solution onto a 1° (longitude) by 0.5° (latitude) grid using a Gaussian weight of all samples within 0.5° distance. The half-width at half-height of the Gaussian weight function is 0.593°. We produce a total of 232 points for the combined geodetic observations at 2° × 1° spacing in longitude and latitude (blue arrows in Figure 2c). We also test our models using a more extensive set of horizontal GNSS measurements (Wright et al., 2023, and references therein, Figure 1b). Excluding GNSS measurement points that are too close to model faults (<10 km) or too close together (<10 km) and have greater uncertainty, we use 2,656 GNSS measurements as constraints.

2.2 Methods

2.2.1 Power Law Rheology in a Faulted Ductile Medium

The vertically-averaged rheology of the TVS is described by a power law relation between deviatoric stress and strain rate (England & McKenzie, 1982; Sonder & England, 1986):

$$\overline{\tau}_{ij} = B\dot{E}^{(\frac{1}{n}-1)}\dot{\varepsilon}_{ij} \tag{1}$$

where $\overline{\tau}_{ij}$ is the ijth component of the deviatoric stress (averaged over the thickness of the lithosphere, L), $\dot{\varepsilon}_{ij}$ is the ijth component of the strain rate tensor (assumed constant with depth), and $\dot{E}$ is the second invariant of the strain rate tensor:

$$\dot{E} = \sqrt{\dot{\varepsilon}_{kl}\dot{\varepsilon}_{kl}} \tag{2}$$

The fluid is assumed to be incompressible ($\dot{\varepsilon}_{kk}$=0). The viscosity coefficient, B, and the power law exponent, n, define the physical properties of the lithosphere. In this study, we use n=3, which is suitable for a lithosphere where depth-averaged rheology is dominated by the power law creep of olivine (Brace & Kohlstedt, 1980; Karato et al., 1986; Kirby & Kronenberg, 1987), whereas large n represents plastic behavior (Goetze et al., 1978). The effective viscosity is

$$\eta_{eff} = \frac{1}{2}B\dot{E}^{(\frac{1}{n}-1)} \tag{3}$$

Note that for non-Newtonian fluids ($n \neq 1$) the effective viscosity is dependent on strain rate. The GPE is calculated assuming local isostatic balance of topography ETOPO1 (Amante & Eakins, 2009) smoothed with a Gaussian filter width of 20 km. The Argand number, Ar, as defined by England and McKenzie (1982), represents the relative importance of gravitational buoyancy related stress to viscous stress required to deform the lithosphere at a reference strain rate $\frac{U_0}{L}$:

$$Ar = \frac{g\rho_c L(1-\frac{\rho_c}{\rho_m})}{B_0(\frac{U_0}{L})^{\frac{1}{n}}} \tag{4}$$

where g is the gravitational acceleration, ρ_c and ρ_m are the average densities of crust and mantle, respectively, B_0 is the scale factor for the viscosity coefficient, and U_0 is a scale velocity determined by minimizing the root mean square (RMS) misfit function:

$$M = [\frac{1}{N}\sum_{i=1}^{N}|\boldsymbol{u_i} - U_0\boldsymbol{u_i}'|^2]^{\frac{1}{2}} \tag{5}$$

where $\boldsymbol{u_i}$ is the ith observed velocity, and $\boldsymbol{u_i}'$ is the dimensionless velocity of the same site in the calculation. In the dimensionless force balance, the Argand number multiplies the lateral gradient of GPE, scaling the force that pushes the layer away from regions of high GPE.

We assume that the continuum deformation may be interrupted by slip on model fault structures, with resistance to displacement proportional to the slip rate for tractions and displacements in the horizontal plane. The depth-averaged shear traction for these model faults is assumed dominated by the behavior of ductile shear zones beneath the seismically active layer. Therefore, we assume for tangential (σ_t) and normal (σ_n) directions:

$$\sigma_t = f_t'\Delta U \tag{6}$$

$$\sigma_n = f_n'\Delta U \tag{7}$$

where f_t' and f_n' represent the dimensionless fault-resistance coefficients in tangential and normal directions, respectively, with zero implying a free-slipping fault and infinity meaning a locked fault. The fault-resistance coefficient has dimensions of stress/velocity, depending on the choice of Ar. Its scale factor is

$$f_0 = \frac{B_0(\frac{U_0}{R})^{\frac{1}{n}}}{U_0} \tag{8}$$

where R is the radius of the Earth.

We explicitly allow for displacement discontinuities across major faults (Altyn Tagh, Haiyuan, Kunlun, Xianshuihe, Sagaing, Main Pamir Thrust faults, and eastern boundary of the Indian Plate) in the India-Asia collision zone where InSAR and GNSS reveal apparent velocity contrasts (Figure 1).

2.2.2 Boundary Conditions and Internal Structures

We use the adapted finite element code BASIL (Houseman et al., 2002) for numerical modeling. The program solves the stress-balance equations using the finite-element method described by Houseman and England (1986) amended to represent a deformation field on a spherical shell, as used by England et al. (2016). Figure 2a shows the boundary conditions. We set velocities to zero along the northern, western, and part of southern boundaries which are assumed fixed to the undeforming Eurasian plate ($U_E = U_N = 0$). We set plate rotations on three boundary sections; we use the reconstructed motion of the Indian Plate relative to Eurasia (IND-EUR) from DeMets et al. (2020) and MORVEL velocities of Yangtze (YZ-EUR) and Amur Plates (AM-EUR) from DeMets et al. (2010). We set the rotation rate of the Indian Plate to 1 (dimensionless) and scale those of Yangtze and Amur Plate boundary segments in proportion. The velocity scale U_0 is determined from the solution by minimizing the misfit (Eq. 5) between observed and dimensionless model velocities. The velocities on the part of the southern boundary that crosses Myanmar are poorly constrained and we set zero velocity in the east direction and zero traction (relative to lithostatic) in the north direction ($U_E = T_N = 0$, Figure 2a); this allows for normal motion along that segment as implied by GNSS measurements in that region (Figure 1b). The complexity of the observed deformation styles indicates the convergence of India with Eurasia is not the only factor influencing the distribution of displacements. The internal buoyancy forces from GPE and heterogeneities in lithospheric strength also contribute to the regional deformation pattern (England & Houseman, 1985; England & Molnar, 2005). Assuming that the background dimensionless depth-averaged viscosity coefficient (B') is 1, we also investigate the influence of regional variations in internal strength by embedding strong Indian Plate, Tarim, Sichuan, and Alxa-Ordos Basins ($B^{'}_S$=10) (Figures 2a and 3a), weakening ($B^{'}_W < 1$) area of high topography defined by the contour of $\sim$ 2,000 m elevation and bounding faults (Figure 4a), and/or central Tibetan Plateau (Figure 5a).

3 Numerical Simulations and Results

We conduct a comprehensive suite of numerical experiments, aiming to match the key features of the geodetic observations (Table 1) under a fixed set of boundary conditions. We incrementally build up the complexity of models in terms of the number of features employed, with the aim to find the most parsimonious solution that matches the large-scale, systematic patterns of the velocity field. In Case 1, we investigate internal strength variations by involving strong Indian Plate, Tarim, Sichuan, and Alxa-Ordos Basins, a weak area of high topography, and/or a weak central Tibetan Plateau. In Case 2, we account for displacement discontinuities by explicitly incorporating faults. In each case we explore the parameter space systematically to obtain a minimum RMS misfit between observations and model horizontal velocities. We compare observed and model gridded eastward velocities for all the experiments as InSAR observations are almost insensitive to north-south motion. However, the InSAR velocity field is also constrained by GNSS measurements of the north component of velocity and our measures of model misfit are equally weighted in both components.

3.1 Case 1: Lateral Heterogeneity in Viscosity Coefficient

3.1.1 Case 1.1: Rigid India Indenter

In this case, we simulate the convergence of India with Eurasia by embedding a rigid Indian Plate in the otherwise homogeneous model domain (Figure 2a). Doing so allows us to apply the present rotation rate vector for India relative to Eurasia (Section 2.2.2) to the arbitrary southern boundary of the domain, in order to produce the apparent motion of the relatively rigid Indian Plate. The depth-averaged viscosity coefficient is set to 10. Because $n = 3$, setting $B^{'}_S$=10 can result in strain rates 10^3 times smaller than

Table 1. Summary of Model Cases to Match the Key Observable Features of the Geodetically-Derived Velocity Field in the India-Asia Convergence Zone

Key observations	Case 1: Lateral heterogeneity in viscosity coefficient				Case 2: Allowing displacements on selected major faults		
	Case 1.1: Rigid India indenter	Case 1.2: Embedding strong Indian plate, Tarim, Sichuan, and Alxa-Ordos basins	Case 1.3: Weakening area of high topography	Case 1.4: Weakening central Tibetan Plateau	Case 2.1: Absence of weak zone	Case 2.2: Embedding weak region of high topography	Case 2.3: Weakening central Tibetan Plateau
Distributed deformation throughout the India-Eurasia collision zone	✓	✓	✓	✓	✓	✓	✓
Dilatation of high plateau	×	×	✓	✓	✓	✓	✓
Contraction on the margins of plateau	Partly	Partly	✓	✓	Partly	✓	✓
Smooth, long-wavelength eastward velocity variation away from major faults	×	×	×	✓	×	×	✓
Strain concentrations on major faults	×	×	Partly	Partly	✓	✓	✓
Asymmetric eastward velocity gradient across the Tibetan Plateau	×	×	Partly	Partly	✓	✓	✓
Clockwise rotation around the EHS	×	×	×	×	✓	✓	✓
Clockwise rotation of the Tarim basin (rotation rate, °/Myr)[a]	-0.149	-0.161	-0.279	-0.274	-0.299	-0.445	-0.413
Best-fit Argand number	1.0	1.8	3.5	4.0	7.4	4.0	4.0
RMS misfit[b]	6.7	6.6	5.9	4.9	5.1	3.8	3.5

[a]The rotation rate is calculated based on model GNSS velocities within the Tarim block for each case, anti-clockwise positive. The rotation rate of the Tarim basin derived from GNSS observations (Figure 1b) is -0.592 °/Myr.
[b]RMS misfit to joint model horizontal velocities of InSAR and GNSS (mm/yr)

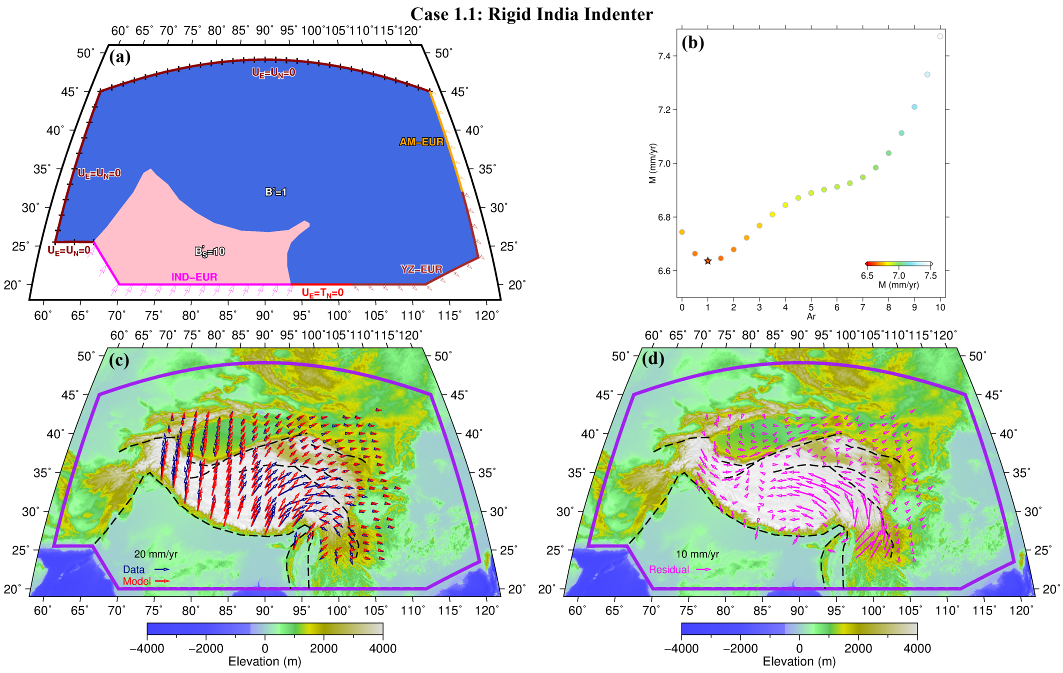

Figure 2. (a) Schematic diagram illustrating boundary conditions and model rheological coefficients for Case 1.1: rigid India indenter. (b) RMS misfit, M, as a function of the Argand number. The mininum misfit is marked as star. (c) Model fits (red arrows) to the sampled observations (blue arrows) from joint model velocities of InSAR and GNSS. Model faults are shown in dashed lines (Figures 2c and 2d), meaning that they are locked (no-slip) in this case. (d) Misfit vectors (model-data).

in an adjoining region where B'=1, though the effect of irregular geometry makes for a more complex dependence of strain-rate on B'_S. The Argand number $Ar = 1$ gives the minimum RMS misfit (6.7 mm/yr, Figure 2b) subject to the choice of $n = 3$ and specified boundary conditions. No displacement is allowed on faults but we observe strain concentrations on the syntaxial regions on either end of the Himalayan chain, and also at points on the external boundary of the domain (Figure S1a), where there is an abrupt change in the boundary conditions. This calculation produces subtle E-W extension/dilatation in the Tibetan Plateau where the ratio of E-W extension rate to N-S convergence rate is around 0.1 (Figures 2c, S1a, and S1b). Clockwise rotation around the EHS is not reproduced (Figure 2c).

3.1.2 Case 1.2: Embedding Strong Indian Plate, Tarim, Sichuan, and Alxa-Ordos Basins

Based on the coherent displacement patterns of the Indian Plate, Tarim, Sichuan, and Alxa-Ordos Basins observed in GNSS dataset, these lithospheric blocks are interpreted to behave as rigid blocks with relatively cold thermal profiles (Tapponnier & Molnar, 1976; Kao et al., 2001; Q. Wang et al., 2001; Yang & Liu, 2002; Jagadeesh & Rai, 2008; C. Li et al., 2008a; P. Zhang & Gan, 2008; Z. Zhang et al., 2010; Craig et al., 2012; Mahesh et al., 2012; C.-L. Zhang et al., 2013; Deng & Tesauro, 2016; Rui & Stamps, 2016). We investigate the impact of involving the four rheologically strong regions, with a viscosity coefficient one order of magnitude higher than background (B'_S=10) (Figure 3a). The outlines of the rigid regions are approximated from the surface geomorphology/topography.

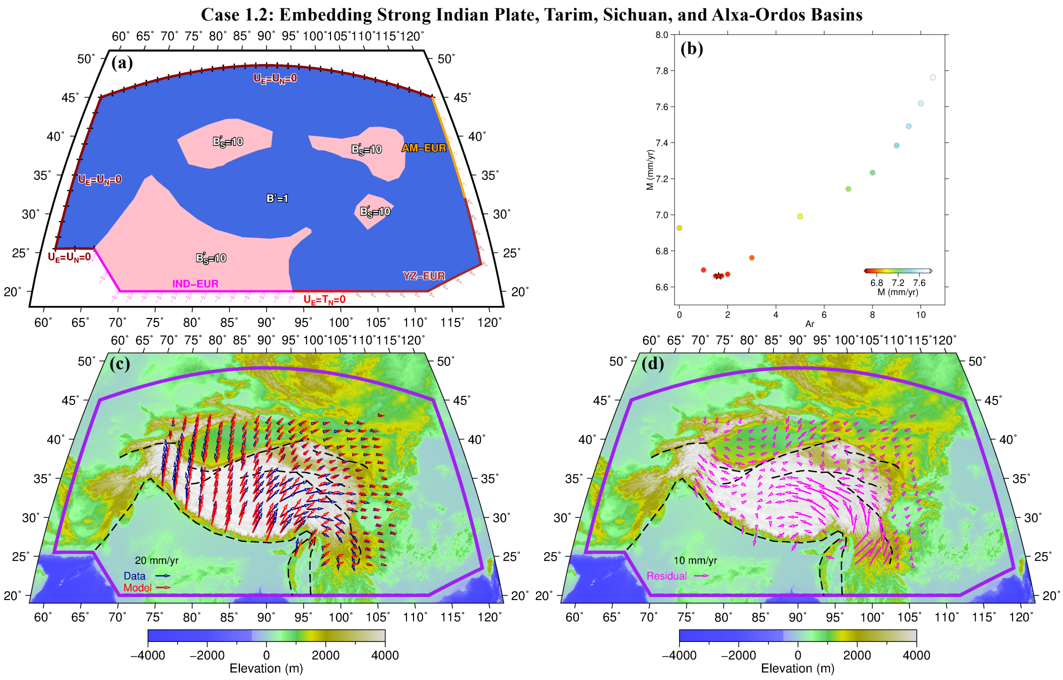

Figure 3. Same as Figure 2, but for Case 1.2: embedding strong Indian Plate, Tarim, Sichuan, and Alxa-Ordos Basins.

In this calculation, the minimum misfit (∼6.6 mm/yr) obtained for Argand number 1.8 (Figure 3b) is comparable to Case 1.1. Asymmetric eastward velocity gradient in the western and eastern Tibetan Plateau and clockwise rotation around the EHS are not recovered (Figure 3c). Negligible strain occurs in the interiors of the rigid blocks (Figures S1c and S1d) and northward displacement rate vectors are still predominant everywhere in the solution domain in contrast to observed eastward rates in the eastern Tibetan Plateau.

3.1.3 Case 1.3: Weakening Area of High Topography

The lithosphere of the Tibetan Plateau and Tian Shan has been suggested to be relatively thinner, hotter and rheologically weaker than the indenting Indian Plate (Tapponnier & Molnar, 1979; Molnar & Tapponnier, 1981). In this case we explore the effect of such weakening regions of high elevation. We choose the shape of the weak region to follow approximately the smoothed contour of ∼2,000 m topography bounded by faults in places (medium blue zone in Figure 4a). We search for an optimal combination of the Argand number and the viscosity coefficient of the weak zone (B'_W). A minimum misfit of 5.9 mm/yr was obtained with Ar of ∼3.5 and B'_W of ∼0.4 (Figure 4b), indicating that gravitational spreading plays a more significant role when enabled by weakened thick crust. It can be seen that there is some trade-off between Ar and B'_W; as Ar increases, a relatively 'stronger' weak zone would be required. This model calculation enhances the expression of eastward motion in the eastern Tibetan Plateau (Figures 4c and S2c). Clockwise rotation around the EHS is still missing (Figure 4c). Note that strain becomes concentrated at regions of strength contrast; this experiment yields nearly E-W extension throughout much of the central-southern Tibetan Plateau and NNW-SSE stretching around the EHS (Figure S1e). The high plateau is dilating, as the weaker plateau is enabled to flow outward from the region of high GPE. The margins of the plateau show convergence (Figure S1f). These patterns are broadly consistent with the geodetically-derived dilatation strain rate field (Wright et al., 2023).

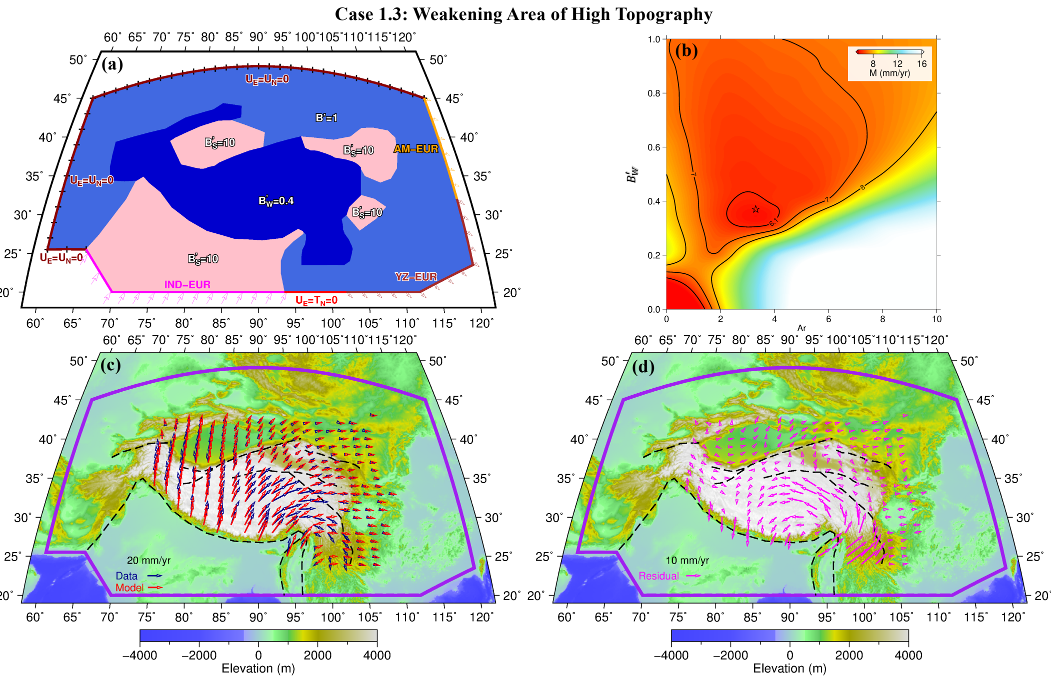

Figure 4. (a) Schematic diagram illustrating boundary conditions and model rheological coefficients for Case 1.3: weakening area of high topography. The weak zone follows the contour of ∼2,000 m elevation bounded by faults in places. (b) Misfit as a function of the Argand number and viscosity coefficient of the weak zone. The minimum misfit is marked as star. Conventions of (c) and (d) are as described in Figure 2.

3.1.4 Case 1.4: Weakening Central Tibetan Plateau

We note that none of the above experiments can produce the observed long-wavelength increase in eastward velocity across the Tibetan Plateau (Figure 6a). We now include in the model an additional rheologically weak central plateau roughly following the shape of the commonly referenced Qiangtang Block (Liu & Yang, 2003; P. Zhang et al., 2003), which is bounded by the Jinsha Suture-Kunlun Fault-Xianshuihe Fault to the north, the Bangong-Nujiang Suture-Jiali Fault-Red River Fault to the south, part of the Karakoram Fault to the west, and the northwestern boundary of the Dianzhong Block to the east (dark blue zone in Figure 5a). As the Dianzhong Block appears to obstruct the material extrusion to the southeast (Han et al., 2022), we exclude the Dianzhong Block from the weak region and keep its viscosity coefficient as that of the background. The misfit is dependent on the Argand number, viscosity coefficients of the weak high topographic area ($B^{'}_{W1}$) and central Tibetan Plateau ($B^{'}_{W2}$). The combination of the three parameters (4.0, 0.5, 0.1, respectively) leads to a minimum misfit of 4.9 mm/yr (Figure 5b), as opposed to 5.9 mm/yr in Case 1.3. This simulation facilitates the eastward velocity gradient across the Tibetan Plateau (Figures 5c, 6a, and S2d). Again, the clockwise rotation around the EHS is not reproduced (Figure 5c). The strain rate fields in this calculation are similar to those of Case 1.3, except for additional strain concentration at regions of strength contrasts (Figures S1g and S1h). The significance of this experiment is that we recover the gradient of eastward velocity across the Tibetan Plateau (~20 mm/yr contrast over ~1,400 km distance, compared to ~10 mm/yr difference over that distance in Case 1.3, Figure 6a).

3.2 Case 2: Allowing Displacements on Selected Major Faults

In Cases 1.3 and 1.4, strain is concentrated at regions of strength contrast (Figures S1e and S1g). As obvious velocity gradients have been observed across major faults in the Tibetan Plateau (Wright et al., 2023, Figure 6), we introduce strain localization on faults by explicitly allowing for displacement discontinuities across the faults in Case 2.

3.2.1 Case 2.1: Absence of Weak Zone

We first exclude any weak regions to investigate the impact of fault-resistance coefficients. We take into account the dominant strike-slip motion along major faults (Altyn Tagh, Haiyuan, Kunlun, and Xianshuihe Faults) by applying a constant strike-parallel fault-resistance coefficient ($f^{'}_t$) along a fault. We also allow dip-slip motion on the eastern boundary of the Indian Plate, the Sagaing Fault, and the Main Pamir Thrust Fault by applying $f^{'}_t$ and $f^{'}_n$ parameters simultaneously. Model faults are delineated as thick black lines in Figure 7a. In this case, we allow Ar and $f^{'}_t$ to be free parameters. To maintain the simplicity of the calculations, we assume a uniform $f^{'}_t$ for all model faults (with the same-magnitude $f^{'}_n$ applied for the Sagaing Fault), and set $f^{'}_n = 10$ for both the eastern boundary of the Indian Plate and the Main Pamir Thrust Fault determined by trial and error (Figure 7a). We obtained a minimum misfit of 5.1 mm/yr with Ar of 7.4 (Figure 7b). The fault-resistance coefficients are at most ~0.2 (Figure 7b), indicating that the faults tend to be free-slipping. This calculation allows discontinuities in the velocity component across faults (Figures 6 and S2e) and reproduces the asymmetric eastward velocity gradient across the Tibetan Plateau (Figure 7c). Relative to previous simulations, Case 2.1 predicts a greater rate of clockwise rotation of the Tarim Basin, owing to shear motion allowed on the Altyn Tagh Fault as its southern boundary. Clockwise rotation around the EHS is also enhanced, due to the model allowing local convergence on the Sagaing Fault and the eastern boundary of the Indian Plate as a rough representation of Indo-Burma subduction. The fault-resistance coefficients determine the velocity steps across the faults (Figure 6). Note that geodetic data constrain short-term interseismic strain rates across locked faults, whereas the geodynamic model is predict-

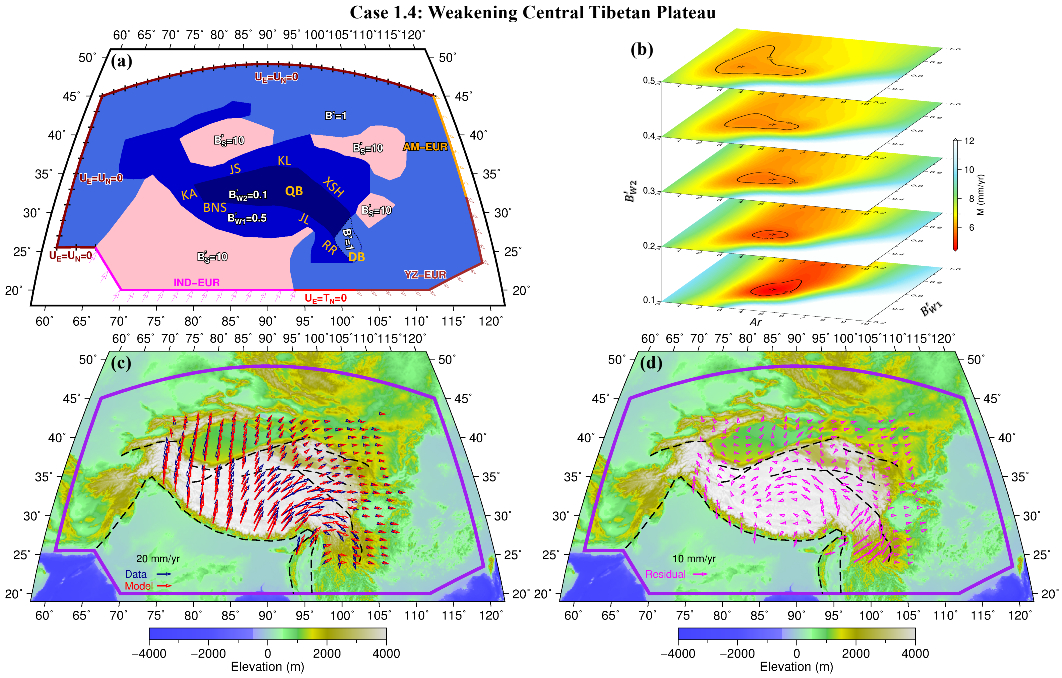

Figure 5. (a) Schematic diagram illustrating boundary conditions and model rheological coefficients for Case 1.4: weakening central Tibetan Plateau. QB = Qiangtang Block, JS = Jinsha Suture, KL = Kunlun Fault, XSH = Xianshuihe Fault, KA = Karakoram Fault, BNS = Bangong-Nujiang Suture, JL = Jiali Fault, RR = Red River Fault. The Dianzhong Block (DB) is delimited by dashed polygon, with viscosity coefficient of 1 as background. (b) RMS misfit as a function of the Argand number, viscosity coefficients of high topographic area ($B^{'}_{W1}$) and central Tibetan Plateau ($B^{'}_{W2}$). Stars denote the best fits for each value of $B^{'}_{W2}$ tested, with the global minimum misfit occurring at $B^{'}_{W2} = 0.1$. Conventions of (c) and (d) are as described in Figure 2.

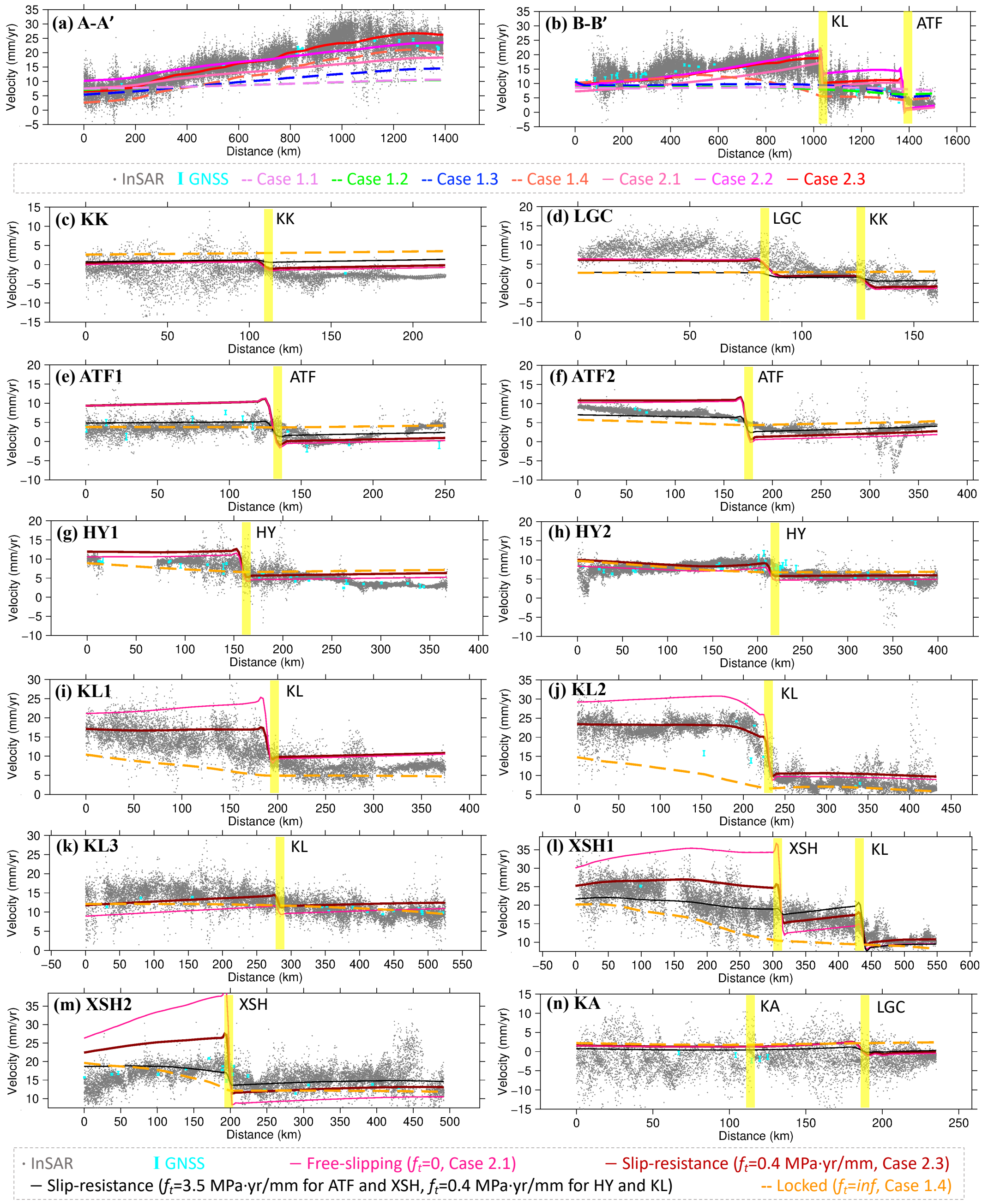

Figure 6. Eastward velocity profiles whose locations and labels are shown in Figure 1a. Velocities from InSAR (within 40 km bin) and GNSS (within 100 km bin) observations are shown as gray dots and cyan dots with 1-sigma error bars, respectively (Wright et al., 2023, and references therein). Yellow bars mark the location of faults. (a, b) Two long profiles nearly perpendicular or parallel to the direction of the India-Asia convergence. Colored lines represent model velocities for each case, among which cases without faults are shown as dashed lines while cases with faults are shown as solid lines. (c-n) Profiles across major strike-slip faults in the Tibetan Plateau showing the effect of the fault-resistance coefficients. Model velocities in cases without faults are shown as orange dashed lines ($f_t = inf$). Pink lines denote faults that are free-slipping ($f_t = 0$). Dark red lines represent faults with uniform resistance to slip ($f_t = 0.4$ MPa·yr/mm) for all model faults. Black lines show larger slip-resistance ($f_t = 3.5$ MPa·yr/mm) for both ATF (including KK and LGC branches) and XSH, with $f_t = 0.4$ MPa·yr/mm for HY and KL. Faults: KK = Karakash Fault, LGC = Longmu-Gozha Co Fault, ATF = Altyn Tagh Fault, HY = Haiyuan Fault, KL = Kunlun Fault, XSH = Xianshuihe Fault, KA = Karakoram Fault.

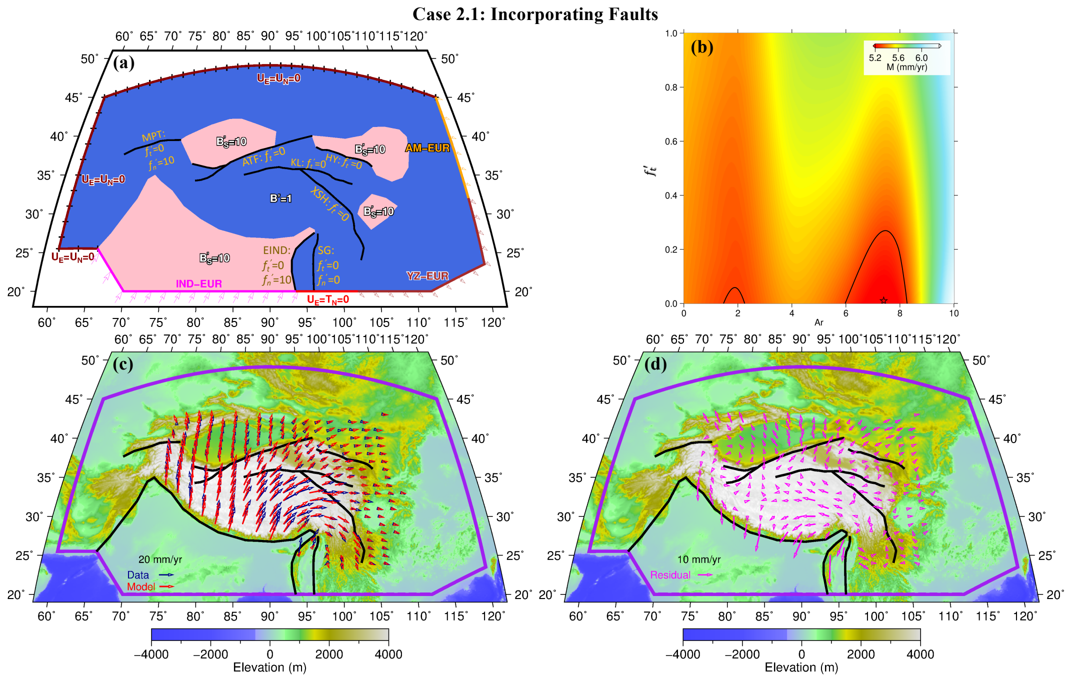

Figure 7. (a) Schematic diagram illustrating boundary conditions and internal structures for Case 2.1: incorporating faults without high-elevation weak zones. Thick black lines denote model faults: MPT = Main Pamir Thrust Fault, ATF = Altyn Tagh Fault, HY = Haiyuan Fault, KL = Kunlun Fault, XSH = Xianshuihe Fault, SG = Sagaing Fault, EIND = eastern boundary of the Indian Plate. $f_t^{'}$ and $f_n^{'}$ are fault-resistance coefficients in tangential and normal directions, respectively. (b) Misfit as a function of the Argand number and fault-resistance coefficient. The best-fit solution has $Ar = 7.4$, $f_t^{'}$=0 and $f_n^{'}$=*inf* for all model faults, except $f_n^{'}$=0 for SG, $f_n^{'}$=10 for MPT and EIND. (c) Model fits (red arrows) to the sampled observations (blue arrows) from joint model velocities of InSAR and GNSS. Model faults are shown in thick black lines. (d) Misfit vectors.

ing long-term velocities and strains averaged over multiple earthquake cycles. To facilitate comparison, we apply a Gaussian filter of width 100 km to the model velocity field to simulate the effect of interseismic locking before calculating the strain rate fields (Figure S3). In this simulation, strain concentrations on major faults and dilatation of high plateau are reproduced (Figures S1i and S1j). However, the NE-SW and nearly E-W convergences on the northeastern and eastern margins of the plateau, respectively, are missing (Figure S1j). The long-wavelength eastward velocity variation away from major faults also is not well captured (Figure 6a).

3.2.2 Case 2.2: Embedding Weak Region of High Topography

We now include (Figure 8a) the weak high-elevation areas along with the faults, as described in Section 3.1.3, in attempting to reproduce the dilatation of high plateau and convergence on the margins of the plateau, especially in the northeastern plateau (Case 1.3, Figure S1f, and Table 1). For a given viscosity coefficient of the weak zone ($B_W^{'}$ of 0.2, 0.4, 0.6, 0.8, and 1), we explore an optimal combination of the Argand number and fault-resistance coefficients. The model favors a $B_W^{'}$ of 0.4 for the weak zone, Ar of ∼4 and $f_t^{'}$ of 0.2, with a misfit of 3.8 mm/yr (Figure 8b). This calculation predicts a gentler eastward velocity gradient (<15 mm/yr contrast over a distance of ∼1,400

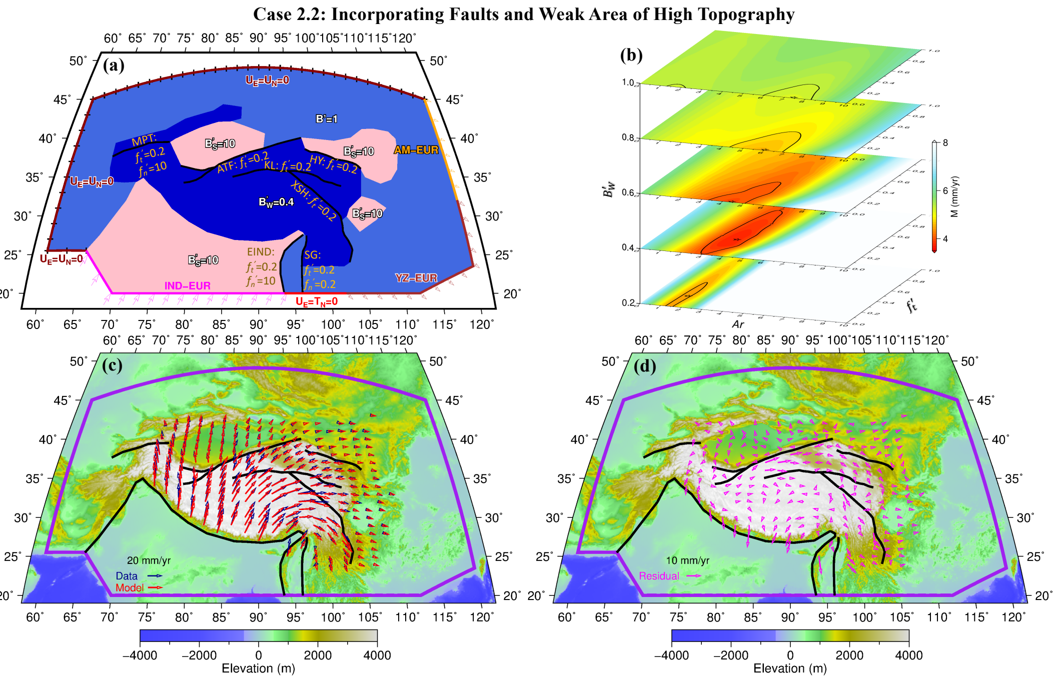

Figure 8. (a) Schematic diagram illustrating boundary conditions and internal structures for Case 2.2: incorporating faults and weak region of high topography. The weak zone is bounded approximately by the ∼2,000 m elevation contour and the major faults. Thick black lines represent model faults: MPT = Main Pamir Thrust Fault, ATF = Altyn Tagh Fault, HY = Haiyuan Fault, KL = Kunlun Fault, XSH = Xianshuihe Fault, SG = Sagaing Fault, EIND = eastern boundary of the Indian Plate. $f_t^{'}$ and $f_n^{'}$ are fault-resistance coefficients in tangential and normal directions, respectively. (b) Misfit as a function of the Argand number, fault-resistance coefficient, and viscosity coefficient of the weak region. Well-matched parameter combinations are shown as stars, with the global minimum misfit occurring at $B_W^{'} = 0.4$. The best-fit solution has $Ar = 4.0$, $f_t^{'}$=0.2 and $f_n^{'}$=inf for all model faults, except $f_n^{'}$=0.2 for SG, $f_n^{'}$=10 for MPT and EIND. Conventions of (c) and (d) are as described in Figure 7.

km) than observed (∼20 mm/yr) (Figure 6a). Other than this, Model 2.2 recovers the key observations listed in Table 1.

3.2.3 Case 2.3: Weakening Central Tibetan Plateau

In this case, we present a hybrid model incorporating both faults and laterally varying viscosity coefficients. Case 1.4 shows weakened central Tibetan Plateau with $B_{W2}^{'}$ of 0.1, which produces the observed smooth, long-wavelength eastward velocity variation across the plateau (Figure 6a). We here search for a best-fit combination of the Argand number, fault-resistance coefficient, and viscosity coefficient of the weak high topographic region ($B_{W1}^{'}$), with $B_{W2}^{'}$ fixed at 0.1 (Figures 9a and 9b). The misfit was reduced to 3.5 mm/yr (Figure 9b). In comparison with Case 2.2, the main improvement of Case 2.3 is that the long-wavelength eastward velocity variation has been well captured, with ∼20 mm/yr gradient over ∼1,400 km (Figure 6a). The model eastward velocity field (Figure 10) and model-derived strain rate fields (Figure 11) show agreement with the geodetic observations (Figures 1 and 11, Wright et al., 2023). This simulation explains all the key features of the India-Eurasia convergence evident in the geodetic ob-

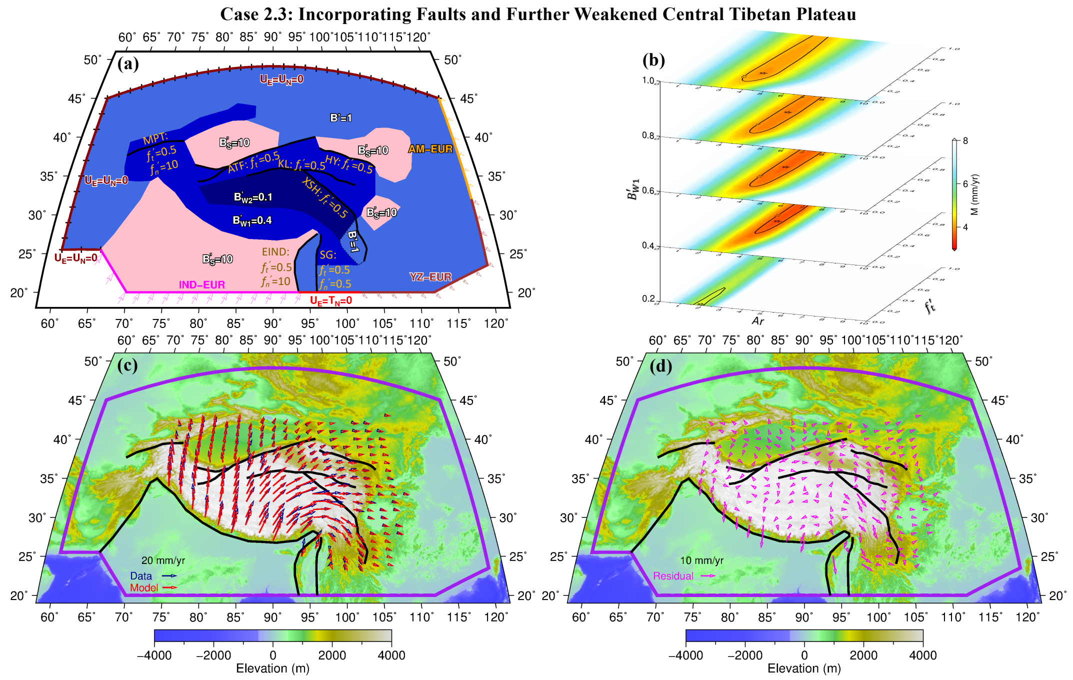

Figure 9. Same as Figure 8, but for Case 2.3: incorporating faults and further weakened central Tibetan Plateau. The best-fit solution has Ar = 4.0, f_t'=0.5 and f_n'=inf for all model faults, except f_n'=0.5 for SG, f_n'=10 for MPT and EIND.

servations (Table 1, Figures 6, 9, 10, and 11). Our results support the finding of Han et al. (2022) that the southeastward lithospheric extrusion is restricted by a relatively strong South China region, which includes the Dianzhong Block.

We also use the published GNSS velocities (Wright et al., 2023, and references therein, Figure 1b) to test our best model (i.e., Case 2.3). Model 2.3 can explain the GNSS observations (Figure 12), with a misfit of 3.8 mm/yr. The individual RMS misfit values for each region are 3.3 mm/yr (Tian Shan and northwestern Tibetan Plateau, Figure 12b), 4.6 mm/yr (plateau interior, Figure 12d), 2.4 mm/yr (northeastern Tibetan Plateau, Figure 12f), and 3.8 mm/yr (southeastern Tibetan Plateau, Figure 12h), respectively. A systematic residual occurs along the Main Himalayan Thrust (Figure 12d), which is likely controlled by relative motion on this structure and is not accounted for in the model (i.e., the Himalayan arc is locked in the numerical experiments). The Burma subduction is roughly represented by the model allowing for local convergence on the Sagaing Fault and eastern boundary of the Indian Plate. However, misfits are clearly visible along these structures (Figure 12h), which is likely due to the simplification of using the faulted TVS model to approximate subduction (Steckler et al., 2008; Artemieva et al., 2016).

4 Discussion

4.1 Slip Resistance on Faults Embedded in a Viscous Continuum

A "fault" in the context of the TVS model represents localized strain that is mediated in part by slip on a near-surface fault and by viscous strain of a narrow ductile shear zone at greater depths. Deformation can be generally represented as a continuum influenced by faults. Continuum deformation may comprise both elastic (e.g., earthquakes) and ductile (e.g., folds and shear zones) behavior. The elastic deformation may be ne-

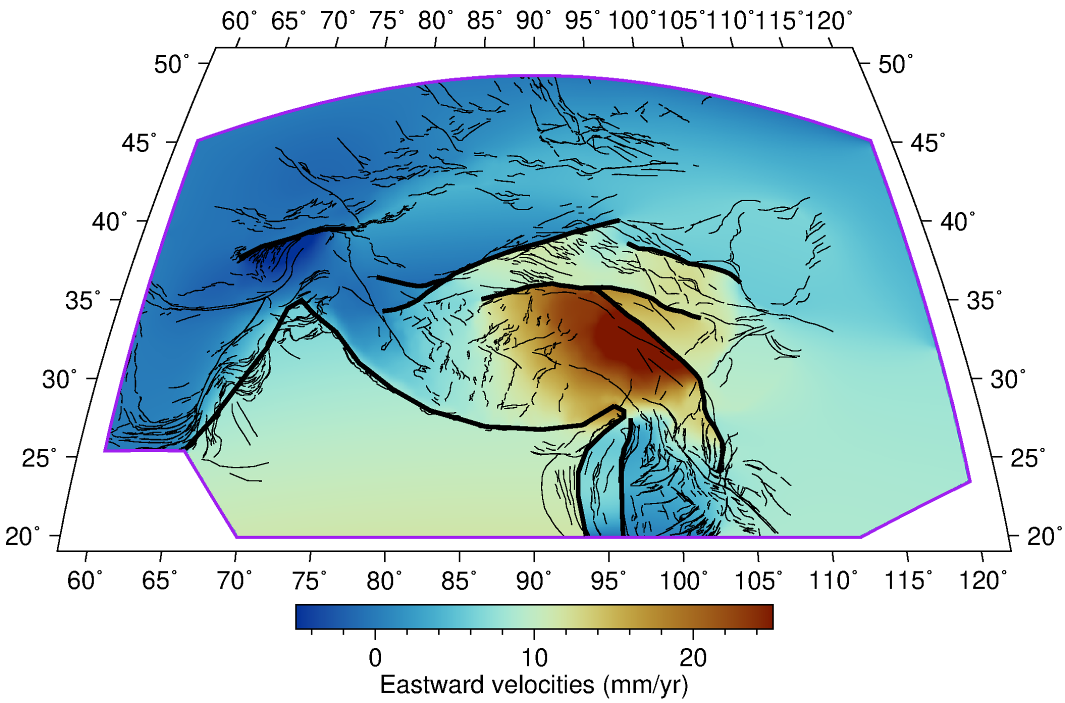

Figure 10. Model eastward component of velocity for Case 2.3, incorporating faults and further weakened central Tibetan Plateau. Model faults are shown as thick black lines. Thin lines denote fault traces from the GEM Global Active Faults Database (Styron & Pagani, 2020).

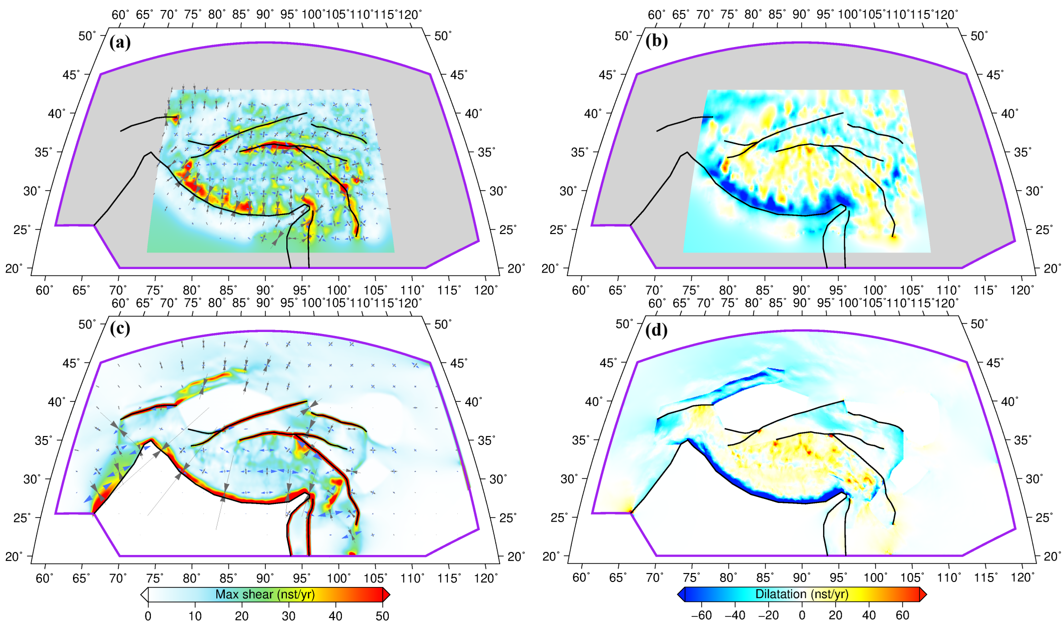

Figure 11. (a) Maximum shear strain rate and (b) dilatation from the geodetically-derived velocity field (Figure 1, Wright et al., 2023). (c) Model-derived maximum shear strain rate from Case 2.3: incorporation of faults and additional weak central Tibetan Plateau. Arrow pairs show principal strain rates, with contraction shown in gray and extension shown in blue. (d) Dilatation strain rate from Case 2.3. nst = 10^{-9}.

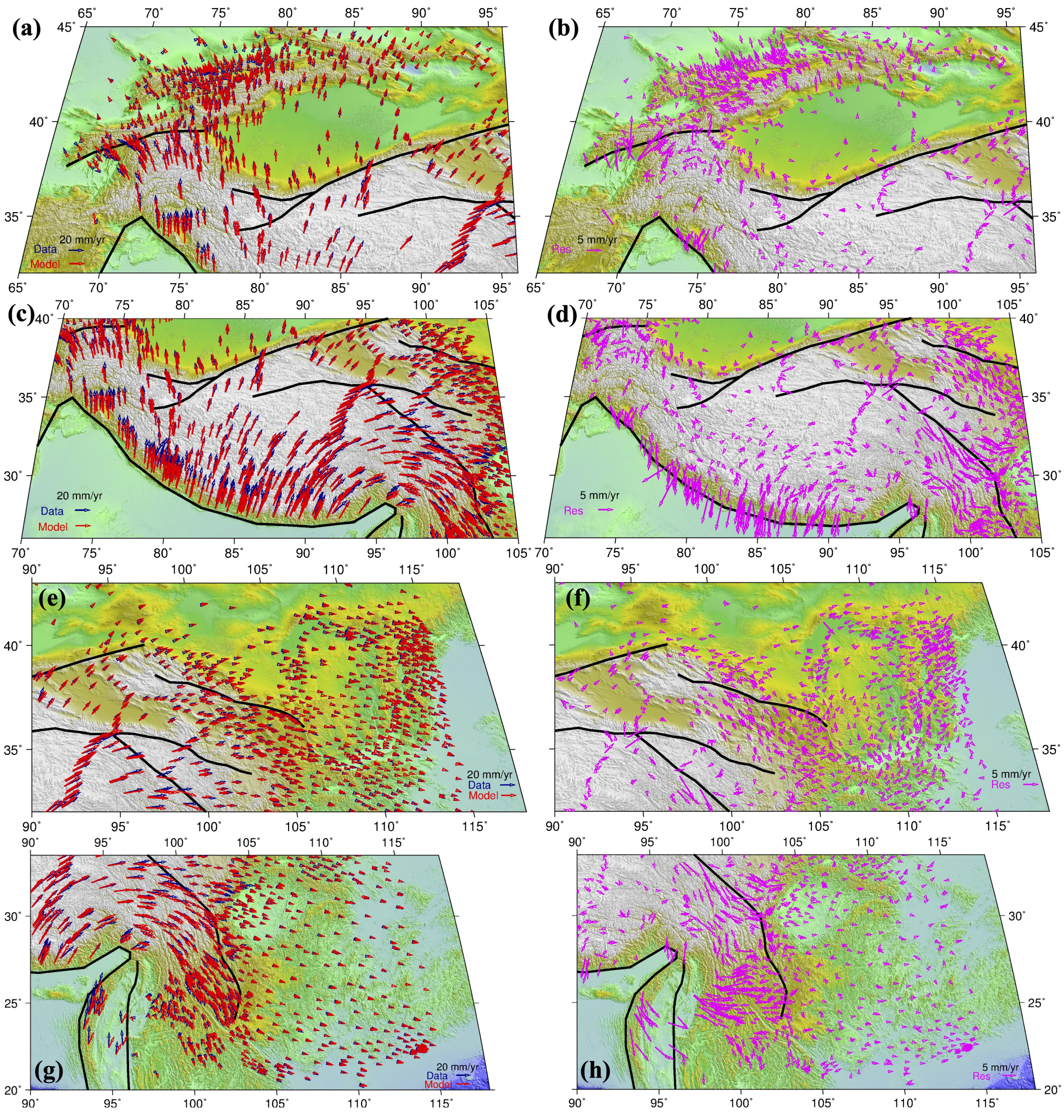

Figure 12. Zoomed view of observed (blue arrows) and model (red arrows) GNSS velocities for the best-fit solution (i.e., Case 2.3) in Tian Shan and northwestern Tibetan Plateau (a), plateau interior (c), northeastern (e), and southeastern plateau (g). The associated residual vectors are shown as magenta arrows in (b), (d), (f), and (h). The individual RMS misfit values for each region are 3.3 mm/yr (b), 4.6 mm/yr (d), 2.4 mm/yr (f), and 3.8 mm/yr (h), respectively. The spatial extents of each panel are indicated in Figure 1b.

glected when averaged over many fault cycles. We assume the ductile deformation can be described by a non-linear (power-law) viscous rheology. Barr and Houseman (1996) introduce faults into a viscous medium by applying zero shear stress on the faults, although the actual shear stress on active faults is poorly constrained. In this study we describe the deformation field in terms of a viscous continuum with faults on which slip is resisted. The dimensional fault-resistance coefficient depends on the choice of Argand number (see Eqs. 4 and 8). In the context of this model, faults can be locked, stress-free, or support a traction that is proportional to the slip rate. Our results show that the best-fit model requires some resistance to slip on faults (Figure 6). Locked faults do not slip and thus they cannot localize strain unless they coincide with strength-contrast boundaries (e.g., the Kunlun and Xianshuihe Faults in Case 1.4, Figures 6i, 6j, 6l, and 6m). Free-slipping faults overestimate the observed velocity steps (e.g., Figures 6e, 6f, 6i, 6j, 6l, and 6m). Our preferred model uses a uniform scaled fault-resistance coefficient of f_t = 0.4 MPa·yr/mm for all model faults subject to the choice of $Ar = 4$ (Case 2.3), although the velocity contrasts appear to be over-predicted across the Altyn Tagh Fault and the Xianshuihe Fault. Applying relatively large resistance coefficients for the two faults (e.g., $f_t = 3.5$ MPa·yr/mm) can improve the fits locally (Figures 6e, 6f, 6l, 6m, and S4).

4.2 Comparison with Previous Dynamic Models of the India-Eurasia Collision

Table 2 shows a compilation of what existing dynamic models of the India-Eurasia collision predict in terms of the key tectonic deformation patterns observed. Our numerical experiments can intrinsically predict large-scale distributed deformation in the India-Eurasia collision zone. The best model (Case 2.3) explains all the key observations from geodesy listed in Table 1 (see Figures 6, 9, 10, 11, and 12). Whilst we are fitting all of the longer-term features, there remain strong features that we are not expecting to fit, as they relate to shorter-timescale earthquake-cycle type processes, such as elastic locking along the Himalayas. The laterally homogeneous viscous sheet model (England & Houseman, 1986) does not predict the E-W extension of the plateau or focused strain around faults, but lithospheric strength discontinuities cause strain concentration (Dayem et al., 2009; Molnar & Dayem, 2010; Lechmann et al., 2014; Bischoff & Flesch, 2019). Our model distribution of effective viscosity (Figure 13) is comparable to those determined by Flesch et al. (2001), Liu and Yang (2003), Copley and McKenzie (2007), and Deng and Tesauro (2016). Our results support the findings of a strong (10^{24} Pa s, Figure 13) Tarim Basin and a weak ($\sim 10^{22}$ Pa s) Tian Shan (Neil & Houseman, 1997). The Tarim Basin appears to behave as a secondary rigid indenter and experiences little internal deformation, but transmits stress and gives rise to local crustal thickening in Tian Shan (Figure 11) (Molnar & Tapponnier, 1975; England & Houseman, 1985; Neil & Houseman, 1997; Huangfu et al., 2021). We find that a relatively weak (10^{22}–10^{23} Pa s) high topographic region (~2,000 m) predicts the dilatation of the highest-elevation region of the Tibetan Plateau and convergence on the margins of the plateau especially in the northeastern plateau (Cases 1.3, 1.4, 2.2, and 2.3, Figures S1f, S1h, S1l, and 11b). Thus the E-W extensional collapse of the plateau may be explained either by increases in surface elevation (Liu & Yang, 2003) and GPE arising from the thermal evolution of thickened continental lithosphere (England & Houseman, 1989), or by a relatively weak Tibetan lithosphere with an average effective viscosity of 10^{21}–10^{22} Pa s (England & Molnar, 1997; Flesch et al., 2001; Liu & Yang, 2003; L. Chen et al., 2017). A weak ($\sim 10^{21}$ Pa s) central Tibetan Plateau bounded by the Dianzhong Block provides an explanation for the smooth, long-wavelength eastward velocity variation away from major faults (Cases 1.4 and 2.3, Figure 6a), consistent with the suggestion that the Dianzhong Block obstructs the lithospheric extrusion in the southeastern Tibetan Plateau (Han et al., 2022). The asymmetric eastward velocity gradient across the Tibetan Plateau is mainly due to the

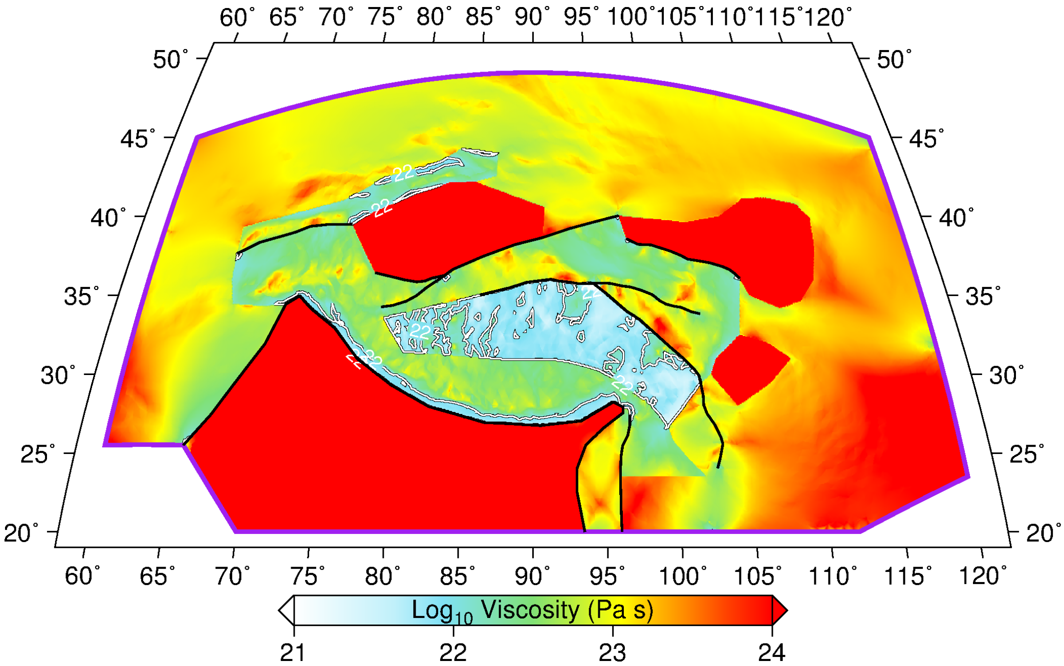

Figure 13. Model distribution of depth-averaged effective viscosity, η_{eff} in Eq. 3, for the best-fit solution (i.e., Case 2.3). Purple line marks the boundary of calculation domain. Thick black lines show model faults. Double lines show the contour of 10^{22} Pa s.

asymmetry of the external boundary conditions (Flesch et al., 2001; Bischoff & Flesch, 2019).

Slip on major faults (Case 2, Figures S1i, S1k, and 11a) and/or lithospheric strength contrasts (Cases 1.3 and 1.4, Figures S1e and S1g, Lechmann et al., 2014; Bischoff & Flesch, 2019) can produce focused strain. The clockwise rotation of the Tarim block (e.g., Avouac & Tapponnier, 1993; Z.-K. Shen et al., 2001; Craig et al., 2012; J. Zhao et al., 2019) is enhanced by motion on the Altyn Tagh Fault (Case 2, Figures 7c, 8c, and 9c); this rotation was not evident in the experiments of Flesch et al. (2001), Liu and Yang (2003), Lechmann et al. (2014), and Bischoff and Flesch (2019) as they did not take account of relative motion on the fault. The clockwise rotation around the EHS was obtained by Bischoff and Flesch (2019) invoking a west-to-east decrease in upper crustal strength. In our numerical simulations, allowing for local convergence on the Sagaing Fault and eastern boundary of the Indian Plate allows the displacement pattern around the EHS to be simulated, and is justified as an approximate characterization of subduction in the Myanmar region (Case 2, Figures 7c, 8c, and 9c, e.g., Steckler et al., 2008).

4.3 Active Faulting and Seismicity

Although the preferred model includes several lithospheric-scale faults on which fault-like displacements are explicitly represented, we also consider that continuous strain within the ductile regions must also be manifest in smaller-scale faulting of the uppermost brittle layer to allow a deformation that is conformable with the continuous strain occurring in the ductile layers beneath. To evaluate the style of faulting expected at any given location we consider the triaxial strain rate field as a sum of two double couples aligned with the principal horizontal strain-rate axes ($\dot{\varepsilon}_1$) and ($\dot{\varepsilon}_2$) (Houseman & England, 1986). The style of faulting that covers the spectrum from normal to strike-slip to

Table 2. Comparison of Dynamic Models Predicting the Key Features of the India-Eurasia Collision

Key observations	2-D modeling				3-D modeling			
	This study (Case 2.3)	England and Houseman (1986)	England and Houseman (1989)	Flesch et al. (2001)	Royden et al. (1997); F. Shen et al. (2001)	Liu and Yang (2003)	Lechmann et al. (2014)	Bischoff and Flesch (2019)
Distributed deformation throughout the India-Eurasia collision zone	✓	✓	✓	✓	✓	✓	✓	✓
Dilatation of high plateau	✓	×	✓	✓	✓	✓	✓	✓
Contraction on the margins of plateau	✓	✓	✓	✓	✓	✓	✓	✓
Smooth, long-wavelength eastward velocity variation away from major faults	✓	–	–	–	–	–	–	–
Strain concentrations on major faults	✓	×	×	×	×	×	✓	✓
Asymmetric eastward velocity gradient across the Tibetan Plateau	✓	–	–	✓	Symmetric	Partly	Symmetric	✓
Clockwise rotation around the EHS	✓	–	–	✓	✓	✓	✓	✓
Clockwise rotation of the Tarim basin	✓	–	–	×	–	×	×	×

reverse faulting can then be described using the parameter p:

$$p = \frac{3}{4} + \frac{1}{\pi} arctan(\frac{\dot{\varepsilon}_2}{\dot{\varepsilon}_1}) \tag{9}$$

When p is in the range $0 \leq p < 0.25$ reverse faulting (RR) is predicted in both principal directions. When $0.25 \leq p < 0.5$ reverse faulting plus subsidiary strike slip (RS) or strike slip plus subsidiary reverse faulting (SR) is predicted, with the transition between RS and SR taking place where $p = 0.375$. Pure strike-slip faulting occurs when $p = 0.5$ and then transitions from strike slip with subsidiary normal faulting (SN) to normal faulting with subsidiary strike slip (NS) and from NS to NN take place at $p = 0.625$ and $p = 0.75$, respectively (Houseman & England, 1986; Gordon & Houseman, 2015; England et al., 2016; Walters et al., 2017).

Figure 14 shows the comparison between the predicted distribution of active faulting and the observed earthquake focal mechanisms. The classification of the focal mechanism data was performed using FMC program according to the values of the P, T, and B Centroid Moment Tensor axes (Álvarez Gómez, 2019). The edges of the plateau are characterized primarily by compressional strain/reverse faulting (Figure 14a). Strike-slip faulting occurs everywhere in the region (Figure 14b). Normal faulting is predicted to dominate in the plateau interior, especially in the southern plateau (Figure 14c). These calculated styles of deformation are in agreement with the distribution of earthquake focal mechanisms (Figure 14d), implying that the faults within the seismogenic upper crust are taking up strain imposed by the ductile lithosphere. This consistency between model prediction and observation validates a key assumption of negligible vertical gradients of horizontal velocities for the TVS model of the India-Eurasia collision in which the deformation field is explained by the balance between gravitational buoyancy forces and stress caused by plate convergence, moderated by a viscous constitutive law.

The TVS approach averages the rheological parameters over the thickness of the lithosphere, and thereby ignores the depth variation of those rheological parameters. We therefore have not considered the class of models in which lower crustal flows at a different rate to the surface (e.g., Royden et al., 1997; Clark & Royden, 2000; Copley & McKenzie, 2007; Royden et al., 2008). For example, Copley and McKenzie (2007) invoked a gravitational flow with rigid base that explains the deformation along the Himalayas and the Indo-Burman Ranges. The vertical partitioning of lithospheric strength is still debated (e.g., Schmalholz et al., 2018; M. Wang et al., 2021). Despite this, our estimate of depth-averaged effective viscosity provides a first-order constraint on the vertical variations of lithospheric strength whatever the depth-dependence of the viscosity profile. The TVS method also treats the lithosphere as a purely viscous medium, as the elastic strain is not represented in the long-term geological record and may be ignored if the inter-seismic strain rate field is representative of the long-term strain (Barr & Houseman, 1996). The simplicity of the TVS approximation allows us to explore the rheology of the lithosphere and gain insights into the behavior of faults in a viscous continuum and the relationship between active faulting and seismicity.

Although relatively complex, our preferred model is necessarily simplified compared to reality, with assumptions like piece-wise constant B' and constant f'. Further fine-tuning of these model parameters or adding additional complexity in boundary conditions might produce a more exact fit to data, particularly along the Himalayan arc and in the southeastern Tibetan Plateau, but would probably not change the broad conclusions reached here. However, possible lateral variations of GPE determined by the thermal evolution of the thickened lithosphere could mitigate the requirement for a very weak central Tibetan Plateau. Apparent misfits are likely controlled by the 3-D nature of collision which is not accounted for in the TVS model (Steckler et al., 2008; Artemieva et al., 2016).

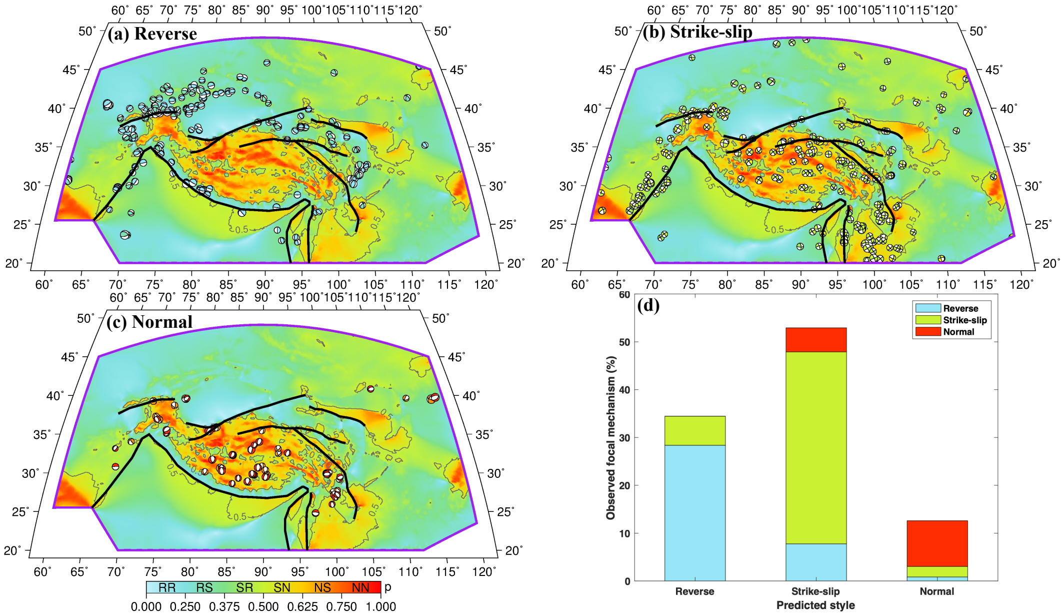

Figure 14. Predicted distribution of fault types compared with observed earthquake focal mechanisms (magnitude≥5.0) from the GCMT catalog (Dziewonski et al., 1981; Ekström et al., 2012). In the two-letter designations, N, S, R, refer to normal, strike-slip, and reverse faulting, with the first letter representing the dominant style of deformation. The $p = 0.5$ contours are shown as gray lines. Purple lines indicate the boundary of the calculation domain. Thick black lines are model faults. (a) Reverse-faulting earthquakes of the region. (b) Strike-slip-faulting earthquakes. (c) Normal-faulting earthquakes. (d) Percentage of earthquake focal mechanisms compared with calculated dominant styles of deformation.

5 Conclusions

We have shown that two-dimensional dynamic models based on a thin viscous shell formulation incorporating discontinuous displacement on major faults can explain the key observations of the India-Eurasia convergence as expressed in the new high-resolution Sentinel-1 InSAR as well as GNSS velocity fields. We conclude that:

(1) The balance between gravitational buoyancy-induced stress and viscous stress shapes the deformation field in the India-Asia collision zone; the preferred model fits the combined geodetic observations with an RMS misfit of 3.5 mm/yr and an Argand number of ∼4.0.

(2) The observed dilatation strain rate field is explained by the inclusion of a relatively weak region of high topography (∼2,000 m) with a depth-averaged effective viscosity of 10^{22}–10^{23} Pa s.

(3) A weak central Tibetan Plateau ($\sim 10^{21}$ Pa s) bounded by the Dianzhong Block replicates the smooth, long-wavelength eastward velocity variation away from major faults.

(4) Shear resistance to slip (0.4 MPa·yr/mm subject to the choice of Ar=4) on major faults allows strain concentration on those systems.

(5) Clockwise rotation around the EHS is produced by the model allowing for local convergence on the eastern boundary of the Indian Plate (7.5 MPa·yr/mm) and the Sagaing Fault (0.4 MPa·yr/mm), approximately representing subduction in the Myanmar region.

Acknowledgments

COMET is the UK Natural Environment Research Council (NERC)'s Centre for the Observation and Modelling of Earthquakes, Volcanoes and Tectonics, a partnership between UK Universities and the British Geological Survey. This study was funded by NERC through the "Looking inside the Continents from Space (LiCS)" large grant to University of Leeds (NE/K010867/1) and COMET National Capability grants 2014/2019/2021. Jin Fang acknowledges the support through a China Scholarship Council-University of Leeds joint scholarship (202006270022). John R. Elliott acknowledges the funding from Royal Society Fellowship grant (URF\R\21106) and Royal Society grant (RF\ERE\210143). Figures were produced using the Generic Mapping Tools (GMT) (Wessel et al., 2013) and Matlab.

References

Alvizuri, C., & Hetényi, G. (2019). Source mechanism of a lower crust earthquake beneath the Himalayas and its possible relation to metamorphism. *Tectonophysics*, *769*, 128153. doi: 10.1016/j.tecto.2019.06.023

Amante, C., & Eakins, B. W. (2009). ETOPO1 arc-minute global relief model: procedures, data sources and analysis.

Artemieva, I., Thybo, H., & Shulgin, A. (2016). Geophysical constraints on geodynamic processes at convergent margins: A global perspective. *Gondwana Research*, *33*, 4-23. doi: 10.1016/j.gr.2015.06.010

Avouac, J.-P., & Tapponnier, P. (1993). Kinematic model of active deformation in central Asia. *Geophysical Research Letters*, *20*(10), 895-898. doi: 10.1029/93GL00128

Barr, T. D., & Houseman, G. A. (1996). Deformation fields around a fault embedded in a non-linear ductile medium. *Geophysical Journal International*, *125*(2), 473-490. doi: 10.1111/j.1365-246X.1996.tb00012.x

Beaumont, C., Jamieson, R. A., Nguyen, M., & Lee, B. (2001). Himalayan tectonics explained by extrusion of a low-viscosity crustal channel coupled to focused surface denudation. *Nature*, *414*(6865), 738-742.

Bendick, R., & Flesch, L. (2013). A review of heterogeneous materials and their implications for relationships between kinematics and dynamics in continents. *Tectonics*, *32*(4), 980-992. doi: 10.1002/tect.20058

Bischoff, S., & Flesch, L. (2018). Normal faulting and viscous buckling in the Tibetan Plateau induced by a weak lower crust. *Nature Communications*, *9*(1), 4952. doi: 10.1038/s41467-018-07312-9

Bischoff, S., & Flesch, L. (2019). Impact of lithospheric strength distribution on India-Eurasia deformation from 3-D geodynamic models. *Journal of Geophysical Research: Solid Earth*, *124*(1), 1084-1105.

Brace, W. F., & Kohlstedt, D. L. (1980). Limits on lithospheric stress imposed by laboratory experiments. *Journal of Geophysical Research: Solid Earth*, *85*(B11), 6248-6252. doi: 10.1029/JB085iB11p06248

Bürgmann, R., & Dresen, G. (2008). Rheology of the lower crust and upper mantle: Evidence from rock mechanics, geodesy, and field observations. *Annual Review of Earth Planetary Sciences*, *36*. doi: 10.1146/annurev.earth.36.031207.124326

Chen, L., Capitanio, F. A., Liu, L., & Gerya, T. V. (2017). Crustal rheology controls on the Tibetan plateau formation during India-Asia convergence. *Nature Communications*, *8*(1), 15992. doi: 10.1038/ncomms15992

Chen, Q., Freymueller, J. T., Wang, Q., Yang, Z., Xu, C., & Liu, J. (2004). A deforming block model for the present-day tectonics of Tibet. *Journal of Geophysical Research: Solid Earth*, *109*(B1). doi: 10.1029/2002JB002151

Clark, M. K., & Royden, L. H. (2000). Topographic ooze: Building the eastern margin of Tibet by lower crustal flow. *Geology*, *28*(8), 703-706.

Copley, A., Avouac, J.-P., & Wernicke, B. P. (2011). Evidence for mechanical coupling and strong Indian lower crust beneath southern Tibet. *Nature*, *472*(7341), 79-81. doi: 10.1038/nature09926

Copley, A., & McKenzie, D. (2007). Models of crustal flow in the India-Asia collision zone. *Geophysical Journal International*, *169*(2), 683-698. doi: 10.1111/j.1365-246X.2007.03343.x

Craig, T. J., Copley, A., & Jackson, J. (2012). Thermal and tectonic consequences of India underthrusting Tibet. *Earth and Planetary Science Letters*, *353*, 231-239.

Dal Zilio, L., Hetényi, G., Hubbard, J., & Bollinger, L. (2021). Building the Himalaya from tectonic to earthquake scales. *Nature Reviews Earth & Environment*, *2*(4), 251–268.

Dayem, K. E., Houseman, G. A., & Molnar, P. (2009). Localization of shear along a lithospheric strength discontinuity: Application of a continuous deformation model to the boundary between Tibet and the Tarim Basin. *Tectonics*, *28*(3). doi: 10.1029/2008TC002264

DeMets, C., Gordon, R. G., & Argus, D. F. (2010). Geologically current plate motions. *Geophysical Journal International*, *181*(1), 1-80. doi: 10.1111/j.1365-246X.2009.04491.x

DeMets, C., Merkouriev, S., & Jade, S. (2020). High-resolution reconstructions and GPS estimates of India–Eurasia and India–Somalia plate motions: 20 Ma to the present. *Geophysical Journal International*, *220*(2), 1149-1171. doi: 10.1093/gji/ggz508

Deng, Y., & Tesauro, M. (2016). Lithospheric strength variations in Mainland China: Tectonic implications. *Tectonics*, *35*(10), 2313-2333. doi: 10.1002/2016TC004272

Dubey, A. K., Singh, A., Kumar, M. R., Jana, N., Sarkar, S., Saikia, D., & Singh, C. (2022). Tomographic Imaging of the Plate Geometry Beneath the Arunachal Himalaya and Burmese Subduction Zones. *Geophysical Research Letters*,

49(8), e2022GL098331. doi: 10.1029/2022GL098331
Duvall, A. R., Clark, M. K., Kirby, E., Farley, K. A., Craddock, W. H., Li, C., & Yuan, D.-Y. (2013). Low-temperature thermochronometry along the Kunlun and Haiyuan Faults, NE Tibetan Plateau: Evidence for kinematic change during late-stage orogenesis. *Tectonics*, *32*(5), 1190-1211. doi: 10.1002/tect.20072
Dziewonski, A. M., Chou, T. A., & Woodhouse, J. H. (1981). Determination of earthquake source parameters from waveform data for studies of global and regional seismicity. *Journal of Geophysical Research: Solid Earth*, *86*(B4), 2825-2852. doi: 10.1029/JB086iB04p02825
Ekström, G., Nettles, M., & Dziewoński, A. (2012). The global CMT project 2004–2010: Centroid-moment tensors for 13,017 earthquakes. *Physics of the Earth and Planetary Interiors*, *200*, 1-9. doi: 10.1016/j.pepi.2012.04.002
England, P., & Houseman, G. (1985). Role of lithospheric strength heterogeneities in the tectonics of Tibet and neighbouring regions. *Nature*, *315*(6017), 297-301. doi: 10.1038/315297a0
England, P., & Houseman, G. (1986). Finite strain calculations of continental deformation: 2. Comparison with the India-Asia Collision Zone. *Journal of Geophysical Research: Solid Earth*, *91*(B3), 3664-3676. doi: 10.1029/JB091iB03p03664
England, P., & Houseman, G. (1989). Extension during continental convergence, with application to the Tibetan Plateau. *Journal of Geophysical Research: Solid Earth*, *94*(B12), 17561-17579. doi: 10.1029/JB094iB12p17561
England, P., Houseman, G., & Nocquet, J.-M. (2016). Constraints from GPS measurements on the dynamics of deformation in Anatolia and the Aegean. *Journal of Geophysical Research: Solid Earth*, *121*(12), 8888-8916. doi: 10.1002/2016JB013382
England, P., & McKenzie, D. (1982). A thin viscous sheet model for continental deformation. *Geophysical Journal International*, *70*(2), 295-321.
England, P., & Molnar, P. (1997). Active Deformation of Asia: From Kinematics to Dynamics. *Science*, *278*(5338), 647. doi: 10.1126/science.278.5338.647
England, P., & Molnar, P. (2005). Late Quaternary to decadal velocity fields in Asia. *Journal of Geophysical Research: Solid Earth*, *110*(B12). doi: 10.1029/2004JB003541
England, P., & Molnar, P. (2015). Rheology of the lithosphere beneath the central and western Tien Shan. *Journal of Geophysical Research: Solid Earth*, *120*(5), 3803-3823. doi: 10.1002/2014JB011733
Flesch, L., Bendick, R., & Bischoff, S. (2018). Limitations on Inferring 3D Architecture and Dynamics From Surface Velocities in the India-Eurasia Collision Zone. *Geophysical Research Letters*, *45*(3), 1379-1386. doi: 10.1002/2017GL076503
Flesch, L., Haines, A. J., & Holt, W. E. (2001). Dynamics of the India-Eurasia collision zone. *Journal of Geophysical Research: Solid Earth*, *106*(B8), 16435-16460. doi: 10.1029/2001JB000208
Gan, W., Molnar, P., Zhang, P., Xiao, G., Liang, S., Zhang, K., ... Zhang, L. (2021). Initiation of Clockwise Rotation and Eastward Transport of Southeastern Tibet Inferred from Deflected Fault Traces and GPS Observations. *GSA Bulletin*. doi: 10.1130/B36069.1
Garthwaite, M. C., & Houseman, G. A. (2011). Validity of the thin viscous sheet approximation in models of continental collision. *Journal of Geophysical Research: Solid Earth*, *116*(B2). doi: 10.1029/2010JB007770
Ge, W.-P., Molnar, P., Shen, Z.-K., & Li, Q. (2015). Present-day crustal thinning in the southern and northern Tibetan Plateau revealed by GPS measurements. *Geophysical Research Letters*, *42*(13), 5227-5235. doi: 10.1002/2015GL064347
Godin, L., Grujic, D., Law, R., & Searle, M. (2006). Channel flow, ductile extru-

sion and exhumation in continental collision zones: an introduction. *Geological Society, London, Special Publications*, *268*(1), 1-23. doi: 10.1144/GSL.SP.2006.268.01.01

Goetze, C., Poirier, J. P., Kelly, A., Cook, A. H., & Greenwood, G. W. (1978). The mechanisms of creep in olivine. *Philosophical Transactions of the Royal Society of London. Series A, Mathematical and Physical Sciences*, *288*(1350), 99-119. doi: 10.1098/rsta.1978.0008

Gordon, R. G., & Houseman, G. A. (2015). Deformation of Indian Ocean lithosphere: Evidence for a highly nonlinear rheological law. *Journal of Geophysical Research: Solid Earth*, *120*(6), 4434-4449. doi: 10.1002/2015JB011993

Grujic, D., Hollister, L. S., & Parrish, R. R. (2002). Himalayan metamorphic sequence as an orogenic channel: insight from Bhutan. *Earth Planetary Science Letters*, *198*(1-2), 177-191. doi: 10.1016/S0012-821X(02)00482-X

Han, C., Huang, Z., Hao, S., Wang, L., Xu, M., & Hammond, J. O. S. (2022). Restricted lithospheric extrusion in the SE Tibetan Plateau: Evidence from anisotropic Rayleigh-wave tomography. *Earth and Planetary Science Letters*, *598*, 117837. doi: 10.1016/j.epsl.2022.117837

Houseman, G., Barr, T. D., & Evans, L. (2002). Diverse Geological Applications For Basil: A 2d Finite-deformation Computational Algorithm. In *EGS General Assembly Conference Abstracts* (p. 5321).

Houseman, G., & England, P. (1986). Finite strain calculations of continental deformation: 1. Method and general results for convergent zones. *Journal of Geophysical Research: Solid Earth*, *91*(B3), 3651-3663. doi: 10.1029/JB091iB03p03651

Huangfu, P., Li, Z.-H., Zhang, K.-J., Fan, W., Zhao, J., & Shi, Y. (2021). India-Tarim Lithospheric Mantle Collision Beneath Western Tibet Controls the Cenozoic Building of Tian Shan. *Geophysical Research Letters*, *48*(14), e2021GL094561. doi: 10.1029/2021GL094561

Jagadeesh, S., & Rai, S. S. (2008). Thickness, composition, and evolution of the Indian Precambrian crust inferred from broadband seismological measurements. *Precambrian Research*, *162*(1), 4-15. doi: 10.1016/j.precamres.2007.07.009

Kao, H., Gao, R., Rau, R.-J., Shi, D., Chen, R.-Y., Guan, Y., & Wu, F. T. (2001). Seismic image of the Tarim basin and its collision with Tibet. *Geology*, *29*(7), 575-578. doi: 10.1130/0091-7613(2001)029⟨0575:SIOTTB⟩2.0.CO;2

Karato, S.-I., Paterson, M. S., & FitzGerald, J. D. (1986). Rheology of synthetic olivine aggregates: Influence of grain size and water. *Journal of Geophysical Research: Solid Earth*, *91*(B8), 8151-8176. doi: 10.1029/JB091iB08p08151

Kelemen, P. B., & Dick, H. J. B. (1995). Focused melt flow and localized deformation in the upper mantle: Juxtaposition of replacive dunite and ductile shear zones in the Josephine peridotite, SW Oregon. *Journal of Geophysical Research: Solid Earth*, *100*(B1), 423-438. doi: 10.1029/94JB02063

Kirby, S. H., & Kronenberg, A. K. (1987). Rheology of the lithosphere: Selected topics. *Reviews of Geophysics*, *25*(6), 1219-1244. doi: 10.1029/RG025i006p01219

Kreemer, C., Blewitt, G., & Klein, E. C. (2014). A geodetic plate motion and Global Strain Rate Model. *Geochemistry, Geophysics, Geosystems*, *15*(10), 3849-3889.

Law, R., Searle, M., & Simpson, R. (2004). Strain, deformation temperatures and vorticity of flow at the top of the Greater Himalayan Slab, Everest Massif, Tibet. *Journal of the Geological Society*, *161*(2), 305-320. doi: 10.1144/0016-764903-047

Lechmann, S. M., Schmalholz, S. M., Hetényi, G., May, D. A., & Kaus, B. J. P. (2014). Quantifying the impact of mechanical layering and underthrusting on the dynamics of the modern India-Asia collisional system with 3-D numerical models. *Journal of Geophysical Research: Solid Earth*, *119*(1), 616-644. doi: 10.1002/2012JB009748

Leloup, P. H., Ricard, Y., Battaglia, J., & Lacassin, R. (1999). Shear heating in continental strike-slip shear zones:model and field examples. *Geophysical Journal International*, *136*(1), 19-40. doi: 10.1046/j.1365-246X.1999.00683.x

Li, C., van der Hilst, R. D., Engdahl, E. R., & Burdick, S. (2008a). A new global model for P wave speed variations in Earth's mantle. *Geochemistry, Geophysics, Geosystems*, *9*(5). doi: 10.1029/2007GC001806

Li, C., van der Hilst, R. D., Meltzer, A. S., & Engdahl, E. R. (2008b). Subduction of the Indian lithosphere beneath the Tibetan Plateau and Burma. *Earth and Planetary Science Letters*, *274*(1), 157-168. doi: 10.1016/j.epsl.2008.07.016

Li, J., Yao, Y., Li, R., Yusan, S., Li, G., Freymueller, J. T., & Wang, Q. (2022). Present-Day Strike-Slip Faulting and Thrusting of the Kepingtage Fold-and-Thrust Belt in Southern Tianshan: Constraints From GPS Observations. *Geophysical Research Letters*, *49*(11), e2022GL099105. doi: 10.1029/2022GL099105

Li, W., Chen, Y., Yuan, X., Xiao, W., & Windley, B. F. (2022). Intracontinental deformation of the Tianshan Orogen in response to India-Asia collision. *Nature Communications*, *13*(1), 3738. doi: 10.1038/s41467-022-30795-6

Li, Y., Liu, M., Li, Y., & Chen, L. (2019). Active crustal deformation in southeastern Tibetan Plateau: The kinematics and dynamics. *Earth and Planetary Science Letters*, *523*, 115708. doi: 10.1016/j.epsl.2019.07.010

Li, Y., Liu, M., Wang, Q., & Cui, D. (2018). Present-day crustal deformation and strain transfer in northeastern Tibetan Plateau. *Earth and Planetary Science Letters*, *487*, 179-189. doi: 10.1016/j.epsl.2018.01.024

Liang, X., Chen, Y., Tian, X., Chen, Y. J., Ni, J., Gallegos, A., … Teng, J. (2016). 3D imaging of subducting and fragmenting Indian continental lithosphere beneath southern and central Tibet using body-wave finite-frequency tomography. *Earth and Planetary Science Letters*, *443*, 162-175. doi: 10.1016/j.epsl.2016.03.029

Liu, M., & Yang, Y. (2003). Extensional collapse of the Tibetan Plateau: Results of three-dimensional finite element modeling. *Journal of Geophysical Research: Solid Earth*, *108*(B8). doi: 10.1029/2002JB002248

Loveless, J. P., & Meade, B. J. (2011). Partitioning of localized and diffuse deformation in the Tibetan Plateau from joint inversions of geologic and geodetic observations. *Earth and Planetary Science Letters*, *303*(1), 11-24. doi: 10.1016/j.epsl.2010.12.014

Mahesh, P., Catherine, J. K., Gahalaut, V. K., Kundu, B., Ambikapathy, A., Bansal, A., … Kalita, S. (2012). Rigid Indian plate: Constraints from GPS measurements. *Gondwana Research*, *22*(3), 1068-1072. doi: 10.1016/j.gr.2012.01.011

McCaffrey, R., Long, M. D., Goldfinger, C., Zwick, P. C., Nabelek, J. L., Johnson, C. K., & Smith, C. (2000). Rotation and plate locking at the Southern Cascadia Subduction Zone. *Geophysical Research Letters*, *27*(19), 3117-3120. doi: 10.1029/2000GL011768

McClusky, S. C., Bjornstad, S. C., Hager, B. H., King, R. W., Meade, B. J., Miller, M. M., … Souter, B. J. (2001). Present day kinematics of the Eastern California Shear Zone from a geodetically constrained block model. *Geophysical Research Letters*, *28*(17), 3369-3372. doi: 10.1029/2001GL013091

McKenzie, D. (1972). Active Tectonics of the Mediterranean Region. *Geophysical Journal International*, *30*(2), 109-185. doi: 10.1111/j.1365-246X.1972.tb02351.x

Meade, B. J., & Hager, B. H. (2005). Block models of crustal motion in southern California constrained by GPS measurements. *Journal of Geophysical Research: Solid Earth*, *110*(B3).

Metzger, S., Gagała, , Ratschbacher, L., Lazecký, M., Maghsoudi, Y., & Schurr, B. (2021). Tajik Depression and Greater Pamir Neotectonics From InSAR Rate Maps. *Journal of Geophysical Research: Solid Earth*, *126*(12), e2021JB022775.

doi: 10.1029/2021JB022775

Metzger, S., Ischuk, A., Deng, Z., Ratschbacher, L., Perry, M., Kufner, S.-K., ... Moreno, M. (2020). Dense GNSS Profiles Across the Northwestern Tip of the India-Asia Collision Zone: Triggered Slip and Westward Flow of the Peter the First Range, Pamir, Into the Tajik Depression. *Tectonics*, *39*(2), e2019TC005797. doi: 10.1029/2019TC005797

Molnar, P., & Dayem, K. E. (2010). Major intracontinental strike-slip faults and contrasts in lithospheric strength. *Geosphere*, *6*(4), 444-467. doi: 10.1130/GES00519.1

Molnar, P., & Deng, Q. (1984). Faulting associated with large earthquakes and the average rate of deformation in central and eastern Asia. *Journal of Geophysical Research: Solid Earth*, *89*(B7), 6203-6227. doi: 10.1029/JB089iB07p06203

Molnar, P., & Tapponnier, P. (1975). Cenozoic tectonics of Asia: effects of a continental collision. *Science*, *189*(4201), 419-426.

Molnar, P., & Tapponnier, P. (1978). Active tectonics of Tibet. *Journal of Geophysical Research: Solid Earth*, *83*(B11), 5361-5375. doi: 10.1029/JB083iB11p05361

Molnar, P., & Tapponnier, P. (1981). A possible dependence of tectonic strength on the age of the crust in Asia. *Earth and Planetary Science Letters*, *52*(1), 107-114. doi: 10.1016/0012-821X(81)90213-2

Neil, E. A., & Houseman, G. A. (1997). Geodynamics of the Tarim Basin and the Tian Shan in central Asia. *Tectonics*, *16*(4), 571-584. doi: 10.1029/97TC01413

Ni, J. F., Guzman-Speziale, M., Bevis, M., Holt, W. E., Wallace, T. C., & Seager, W. R. (1989). Accretionary tectonics of Burma and the three-dimensional geometry of the Burma subduction zone. *Geology*, *17*(1), 68-71. doi: 10.1130/0091-7613(1989)017⟨0068:ATOBAT⟩2.3.CO;2

Ou, Q., Daout, S., Weiss, J. R., Shen, L., Lazecký, M., Wright, T. J., & Parsons, B. E. (2022). Large-Scale Interseismic Strain Mapping of the NE Tibetan Plateau From Sentinel-1 Interferometry. *Journal of Geophysical Research: Solid Earth*, *127*(6), e2022JB024176. doi: 10.1029/2022JB024176

Penney, C., & Copley, A. (2021). Lateral Variations in Lower Crustal Strength Control the Temporal Evolution of Mountain Ranges: Examples From South-East Tibet. *Geochemistry, Geophysics, Geosystems*, *22*(2), e2020GC009092. doi: 10.1029/2020GC009092

Rey, P. F., Teyssier, C., & Whitney, D. L. (2010). Limit of channel flow in orogenic plateaux. *Lithosphere*, *2*(5), 328-332. doi: 10.1130/L114.1

Royden, L. H., Burchfiel, B. C., King, R. W., Wang, E., Chen, Z., Shen, F., & Liu, Y. (1997). Surface deformation and lower crustal flow in eastern Tibet. *Science*, *276*(5313), 788-790.

Royden, L. H., Burchfiel, B. C., & van der Hilst, R. D. (2008). The Geological Evolution of the Tibetan Plateau. *Science*, *321*(5892), 1054-1058. doi: 10.1126/science.1155371

Rui, X., & Stamps, D. S. (2016). Present-day kinematics of the eastern Tibetan Plateau and Sichuan Basin: Implications for lower crustal rheology. *Journal of Geophysical Research: Solid Earth*, *121*(5), 3846-3866. doi: 10.1002/2016JB012839

Schmalholz, S. M., Duretz, T., Hetényi, G., & Medvedev, S. (2018). Distribution and magnitude of stress due to lateral variation of gravitational potential energy between Indian lowland and Tibetan plateau. *Geophysical Journal International*, *216*(2), 1313-1333. doi: 10.1093/gji/ggy463

Scholz, C. H., & Choi, E. (2022). What comes first: The fault or the ductile shear zone? *Earth and Planetary Science Letters*, *577*, 117273. doi: 10.1016/j.epsl.2021.117273

Searle, M., Elliott, J., Phillips, R., & Chung, S.-L. (2011). Crustal–lithospheric structure and continental extrusion of Tibet. *Journal of the Geological Society*, *168*(3), 633-672. doi: 10.1144/0016-76492010-139

Searle, M., Law, R., & Jessup, M. (2006). Crustal structure, restoration and evolution of the Greater Himalaya in Nepal-South Tibet: implications for channel flow and ductile extrusion of the middle crust. *Geological Society, London, Special Publications*, *268*(1), 355-378. doi: 10.1144/GSL.SP.2006.268.01.17

Searle, M., Simpson, R., Law, R., Parrish, R., & Waters, D. (2003). The structural geometry, metamorphic and magmatic evolution of the Everest massif, High Himalaya of Nepal–South Tibet. *Journal of the Geological Society*, *160*(3), 345-366. doi: 10.1144/0016-764902-126

Searle, M., & Szulc, A. G. (2005). Channel flow and ductile extrusion of the high Himalayan slab-the Kangchenjunga–Darjeeling profile, Sikkim Himalaya. *Journal of Asian Earth Sciences*, *25*(1), 173-185. doi: 10.1016/j.jseaes.2004.03.004

Shen, F., Royden, L. H., & Burchfiel, B. C. (2001). Large-scale crustal deformation of the Tibetan Plateau. *Journal of Geophysical Research: Solid Earth*, *106*(B4), 6793-6816. doi: 10.1029/2000JB900389

Shen, Z., Lü, J., Wang, M., & Bürgmann, R. (2005). Contemporary crustal deformation around the southeast borderland of the Tibetan Plateau. *Journal of Geophysical Research: Solid Earth*, *110*(B11). doi: 10.1029/2004JB003421

Shen, Z.-K., Wang, M., Li, Y., Jackson, D. D., Yin, A., Dong, D., & Fang, P. (2001). Crustal deformation along the Altyn Tagh fault system, western China, from GPS. *Journal of Geophysical Research: Solid Earth*, *106*(B12), 30607-30621. doi: 10.1029/2001JB000349

Socquet, A., Simons, W., Vigny, C., McCaffrey, R., Subarya, C., Sarsito, D., ... Spakman, W. (2006). Microblock rotations and fault coupling in SE Asia triple junction (Sulawesi, Indonesia) from GPS and earthquake slip vector data. *Journal of Geophysical Research: Solid Earth*, *111*(B8). doi: 10.1029/2005JB003963

Sonder, L. J., & England, P. (1986). Vertical averages of rheology of the continental lithosphere: relation to thin sheet parameters. *Earth and Planetary Science Letters*, *77*(1), 81-90. doi: 10.1016/0012-821X(86)90134-2

Steckler, M. S., Akhter, S. H., & Seeber, L. (2008). Collision of the Ganges–Brahmaputra Delta with the Burma Arc: Implications for earthquake hazard. *Earth and Planetary Science Letters*, *273*(3), 367-378. doi: 10.1016/j.epsl.2008.07.009

Styron, R. (2022). Contemporary Slip Rates of All Active Faults in the Indo-Asian Collision Zone [Preprint]. *ESSOAr*. doi: 10.1002/essoar.10512747.1

Styron, R., & Pagani, M. (2020). The GEM Global Active Faults Database. *Earthquake Spectra*, *36*(1_suppl), 160-180. doi: 10.1177/8755293020944182

Tapponnier, P., & Molnar, P. (1976). Slip-line field theory and large-scale continental tectonics. *Nature*, *264*(5584), 319-324. doi: 10.1038/264319a0

Tapponnier, P., & Molnar, P. (1979). Active faulting and cenozoic tectonics of the Tien Shan, Mongolia, and Baykal Regions. *Journal of Geophysical Research: Solid Earth*, *84*(B7), 3425-3459. doi: 10.1029/JB084iB07p03425

Thatcher, W. (2007). Microplate model for the present-day deformation of Tibet. *Journal of Geophysical Research: Solid Earth*, *112*(B1). doi: 10.1029/2005JB004244

Thatcher, W. (2009). How the continents deform: The evidence from tectonic geodesy. *Annual Review of Earth Planetary Sciences*, *37*. doi: 10.1146/annurev.earth.031208.100035

Thybo, H., Perchuć, E., & Zhou, S. (2000). Intraplate earthquakes and a seismically defined lateral transition in the upper mantle. *Geophysical Research Letters*, *27*(23), 3953-3956. doi: 10.1029/2000GL011636

Vauchez, A., Tommasi, A., & Mainprice, D. (2012). Faults (shear zones) in the Earth's mantle. *Tectonophysics*, *558-559*, 1-27. doi: 10.1016/j.tecto.2012.06

.006

Vergnolle, M., Calais, E., & Dong, L. (2007). Dynamics of continental deformation in Asia. *Journal of Geophysical Research: Solid Earth*, *112*(B11).

Wallace, L. M., McCaffrey, R., Beavan, J., & Ellis, S. (2005). Rapid microplate rotations and backarc rifting at the transition between collision and subduction. *Geology*, *33*(11), 857-860. doi: 10.1130/G21834.1

Wallace, L. M., Stevens, C., Silver, E., McCaffrey, R., Loratung, W., Hasiata, S., … Taugaloidi, J. (2004). GPS and seismological constraints on active tectonics and arc-continent collision in Papua New Guinea: Implications for mechanics of microplate rotations in a plate boundary zone. *Journal of Geophysical Research: Solid Earth*, *109*(B5). doi: 10.1029/2003JB002481

Walters, R. J., England, P. C., & Houseman, G. A. (2017). Constraints from GPS measurements on the dynamics of the zone of convergence between Arabia and Eurasia. *Journal of Geophysical Research: Solid Earth*, *122*(2), 1470-1495. doi: 10.1002/2016JB013370

Wang, H., & Wright, T. J. (2012). Satellite geodetic imaging reveals internal deformation of western Tibet. *Geophysical Research Letters*, *39*(7). doi: 10.1029/2012GL051222

Wang, H., Wright, T. J., Liu-Zeng, J., & Peng, L. (2019). Strain Rate Distribution in South-Central Tibet From Two Decades of InSAR and GPS. *Geophysical Research Letters*, *46*(10), 5170-5179. doi: 10.1029/2019GL081916

Wang, M., & Shen, Z.-K. (2020). Present-Day Crustal Deformation of Continental China Derived From GPS and Its Tectonic Implications. *Journal of Geophysical Research: Solid Earth*, *125*(2), e2019JB018774. doi: 10.1029/2019JB018774

Wang, M., Shen, Z.-K., Wang, Y.-Z., Bürgmann, R., Wang, F., Zhang, P.-Z., … Xue, L. (2021). Postseismic Deformation of the 2008 Wenchuan Earthquake Illuminates Lithospheric Rheological Structure and Dynamics of Eastern Tibet. *Journal of Geophysical Research: Solid Earth*, *126*(9), e2021JB022399. doi: 10.1029/2021JB022399

Wang, Q., Zhang, P.-Z., Freymueller, J. T., Bilham, R., Larson, K. M., You, X., … Liu, J. (2001). Present-day crustal deformation in China constrained by global positioning system measurements. *Science*, *294*(5542), 574-577.

Wang, W., Qiao, X., & Ding, K. (2021). Present-day kinematics in southeastern Tibet inferred from GPS measurements. *Journal of Geophysical Research: Solid Earth*, *126*, e2020JB021305. doi: 10.1029/2020JB021305

Wang, W., Qiao, X., Yang, S., & Wang, D. (2017). Present-day velocity field and block kinematics of Tibetan Plateau from GPS measurements. *Geophysical Journal International*, *208*(2), 1088-1102. doi: 10.1093/gji/ggw445

Warner, M. (1990). Basalts, water, or shear zones in the lower continental crust? *Tectonophysics*, *173*(1), 163-174. doi: 10.1016/0040-1951(90)90214-S

Wessel, P., Smith, W. H. F., Scharroo, R., Luis, J., & Wobbe, F. (2013). Generic Mapping Tools: Improved Version Released. *Eos, Transactions American Geophysical Union*, *94*(45), 409–410. doi: 10.1002/2013EO450001

Wright, T., Elliott, J., Fang, J., Hooper, A., Houseman, G., Lazecky, M., … Zheng, G. (2022). The Dynamics of the India-Asia collision revealed by Geodetic Imaging of the Tibetan plateau. In *EGU General Assembly Conference Abstracts* (pp. EGU22–1675).

Wright, T., Elliott, J. R., Wang, H., & Ryder, I. (2013). Earthquake cycle deformation and the Moho: Implications for the rheology of continental lithosphere. *Tectonophysics*, *609*, 504-523. doi: 10.1016/j.tecto.2013.07.029

Wright, T., Fang, J., Ou, Q., Hooper, A., Lazecky, M., Maghsoudi, Y., … Parsons, B. (2021). How does Tibet deform? A high-resolution 3D velocity field for the India-Eurasia collision from Sentinel-1 InSAR and GNSS. In *AGU Fall Meeting Abstracts* (Vol. 2021, pp. G22A–04).

Wright, T., Houseman, G., Fang, J., Maghsoudi, Y., Hooper, A., Elliott, J., ... Wang, H. (2023). High-resolution geodetic strain rate field reveals internal deformation of Tibetan Plateau. *submitted to Science (available at EarthArXiv.org)*.

Yang, Y., & Liu, M. (2002). Cenozoic deformation of the Tarim plate and the implications for mountain building in the Tibetan Plateau and the Tian Shan. *Tectonics*, *21*(6), 9-1-9-17. doi: 10.1029/2001TC001300

Zhang, C.-L., Zou, H.-B., Li, H.-K., & Wang, H.-Y. (2013). Tectonic framework and evolution of the Tarim Block in NW China. *Gondwana Research*, *23*(4), 1306-1315. doi: 10.1016/j.gr.2012.05.009

Zhang, H., Kirby, E., Li, H., Cook, K., & Zhang, P. (2020). Ten Years After the Wenchuan Earthquake: New Insights Into the Geodynamics of the Eastern Tibet. *Tectonics*, *39*(6), e2020TC006215. doi: 10.1029/2020TC006215

Zhang, P. (2013). A review on active tectonics and deep crustal processes of the Western Sichuan region, eastern margin of the Tibetan Plateau. *Tectonophysics*, *584*, 7-22. doi: 10.1016/j.tecto.2012.02.021

Zhang, P., Deng, Q., Zhang, G., Ma, J., Gan, W., Min, W., ... Wang, Q. (2003). Strong Earthquakes and Active Blocks in Mainland China. *Science in China: Series D (in Chinese)*, *33*(B04), 12-20.

Zhang, P., & Gan, W. (2008). Combined model of rigid-block motion with continuous deformation: Patterns of present-day deformation in continental China. In B. C. Burchfiel & E. Wang (Eds.), *Investigations into the Tectonics of the Tibetan Plateau* (Vol. 444, p. 0). Geological Society of America. doi: 10.1130/2008.2444(04)

Zhang, Z., Yuan, X., Chen, Y., Tian, X., Kind, R., Li, X., & Teng, J. (2010). Seismic signature of the collision between the east Tibetan escape flow and the Sichuan Basin. *Earth and Planetary Science Letters*, *292*(3), 254-264. doi: 10.1016/j.epsl.2010.01.046

Zhao, J., Zhang, P., Yuan, X., Gan, W., Sun, J., Deng, T., ... Teng, J. (2019). Clockwise rotation of the Tarim basin driven by the Indian plate impact. *Earth sciences and subsoil use*, *42*(4), 425-436. doi: 10.21285/2686-9993-2019-42-4-425-436

Zhao, W., & Morgan, W. J. (1987). Injection of Indian crust into Tibetan lower crust: A two-dimensional finite element model study. *Tectonics*, *6*(4), 489-504.

Zheng, G., Wang, H., Wright, T. J., Lou, Y., Zhang, R., Zhang, W., ... Wei, N. (2017). Crustal Deformation in the India-Eurasia Collision Zone From 25 Years of GPS Measurements. *Journal of Geophysical Research: Solid Earth*, *122*(11), 9290-9312. doi: 10.1002/2017JB014465

Zhu, Y., Diao, F., Wang, R., Hao, M., Shao, Z., & Xiong, X. (2022). Crustal Shortening and Rheological Behavior Across the Longmen Shan Fault, Eastern Margin of the Tibetan Plateau. *Geophysical Research Letters*, *49*(11), e2022GL098814. doi: 10.1029/2022GL098814

Álvarez Gómez, J. A. (2019). FMC—Earthquake focal mechanisms data management, cluster and classification. *SoftwareX*, *9*, 299-307. doi: 10.1016/j.softx.2019.03.008

Supporting Information for "The Dynamics of the India-Eurasia Collision: Faulted Viscous Continuum Models Constrained by High-Resolution Sentinel-1 InSAR and GNSS Velocities"

Jin Fang[1], Gregory A. Houseman[1], Tim J. Wright[1], Lynn A. Evans[2], Tim J. Craig[1], John R. Elliott[1], and Andy Hooper[1]

[1]COMET, School of Earth and Environment, University of Leeds, Leeds, United Kingdom

[2]School of Earth, Atmosphere and Environment, Monash University, Clayton, Australia

Contents of this file

Corresponding author: J. Fang, COMET, School of Earth and Environment, University of Leeds, Leeds, United Kingdom. (eejf@leeds.ac.uk)

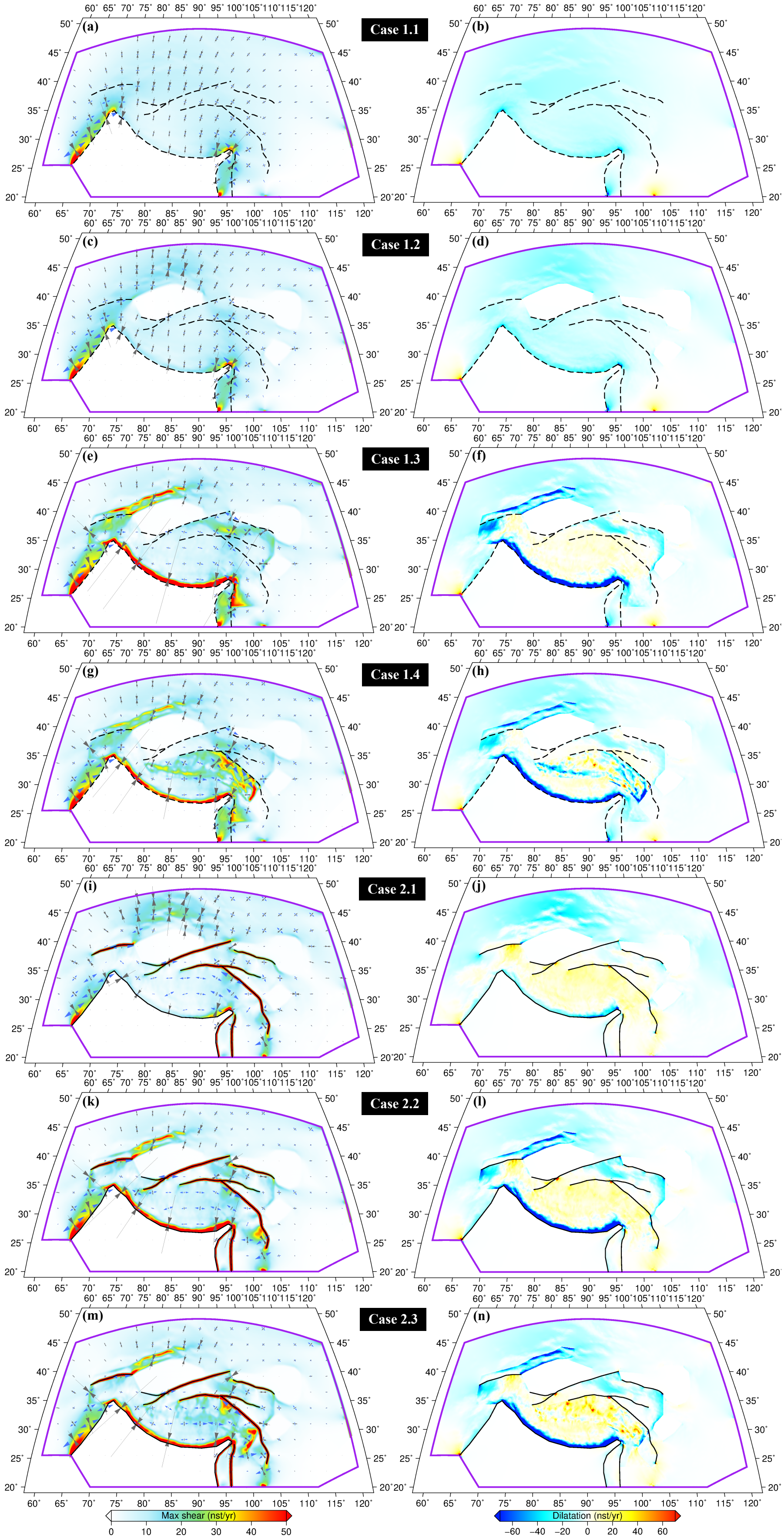

Figure S1. (a, c, e, g, i, k, m) Model-derived maximum shear strain rate from each case. Arrow pairs show principal strain rates, with contraction shown in gray and extension shown in blue. (b, d, f, h, j, l, n) Dilatation strain rates from the models.

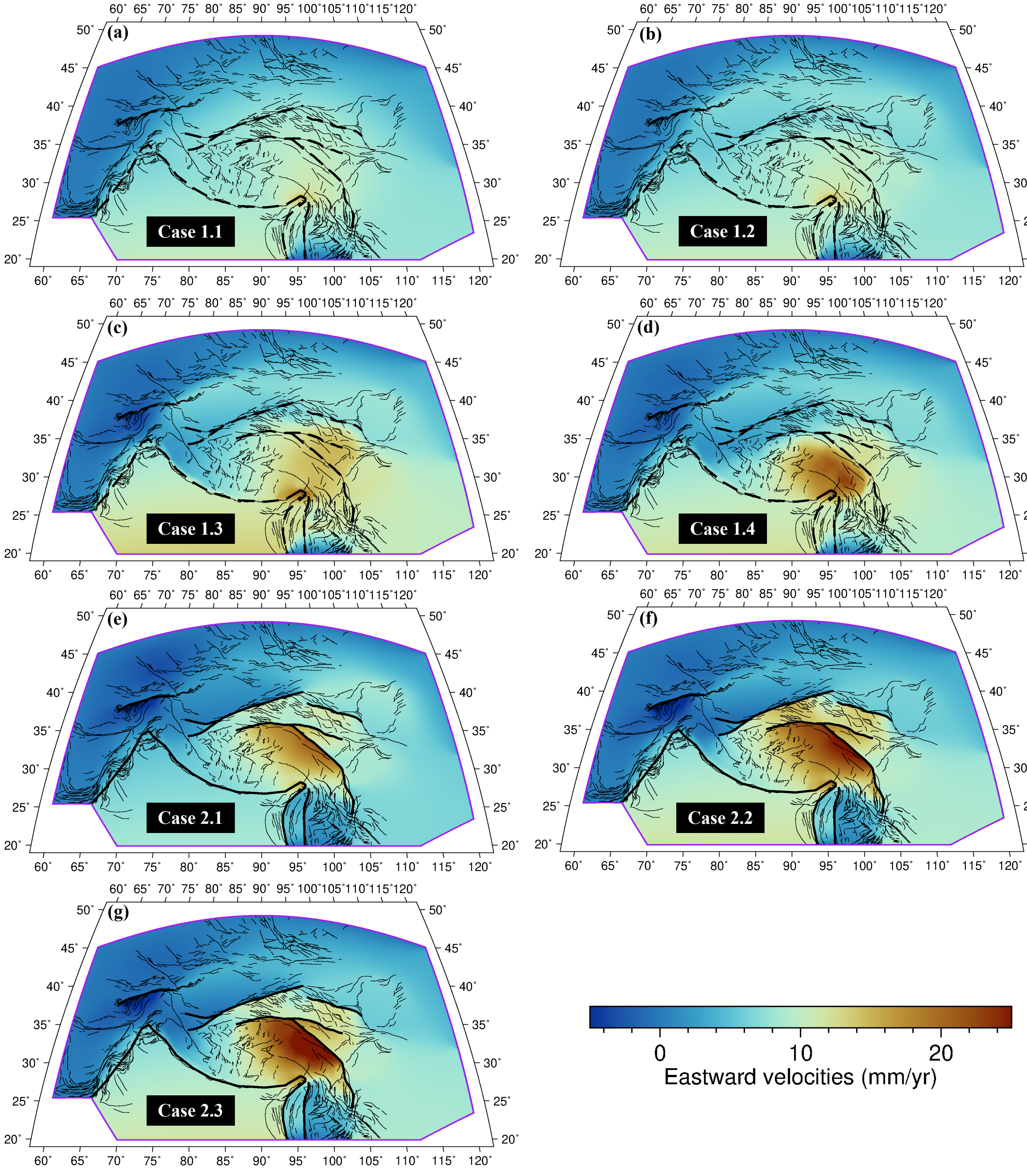

Figure S2. Model eastward velocity fields for each experiment.

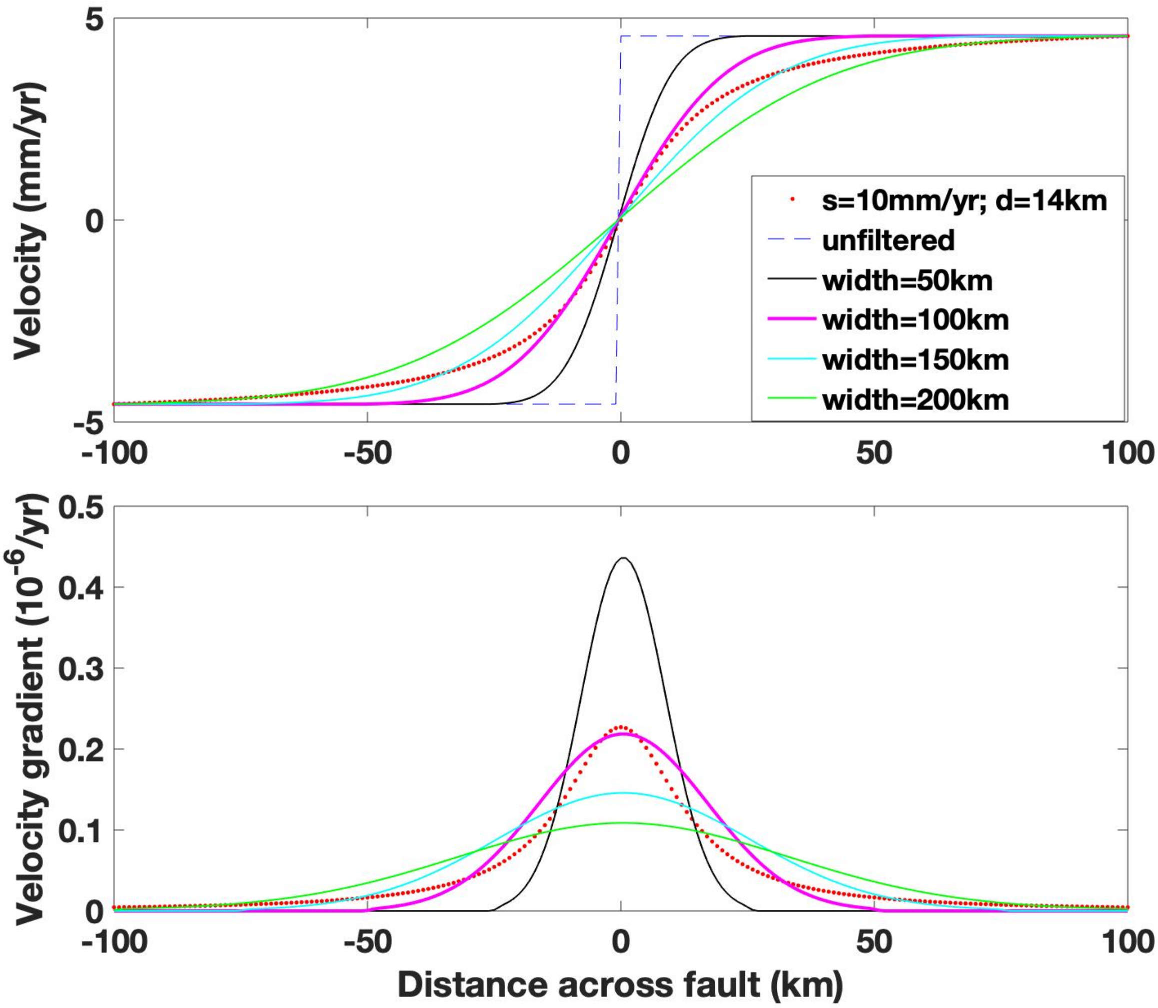

Figure S3. Test of Gaussian filtering width to capture the velocity gradient across a fault. Blue dashed line denotes a representative velocity profile from the dynamic model. Red dotted line represents an arctan-shape velocity profile for a fault with a slip rate of 10 mm/yr and a locking depth of 14 km. Solid lines show different filter widths applied. A width of 100 km (magenta line) best approximates the velocity gradient.

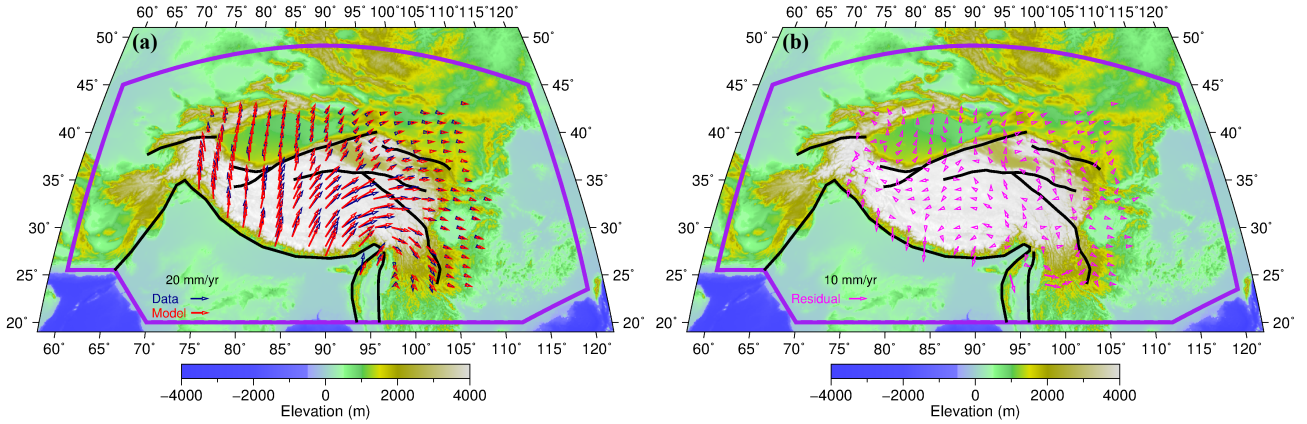

Figure S4. (a) Fits to observations from the calculation with relatively large fault-resistance coefficients (f_t = 3.5 MPa·yr/mm) applied to the Altyn Tagh Fault and the Xianshuihe Fault, and f_t = 0.4 MPa·yr/mm for the rest of model faults. Other parameter settings are kept the same as Case 2.3. (b) Associated residual vectors.